ABSTRACT

ANALYSIS OF TISSUE ENGINEERING STRATEGIES
FOR BONE-RELATED APPLICATIONS

by
Timothy Buirkle

Over the past few decades, tissue engineering approaches have pushed their way to the forefront of biotechnological research and development, serving a wide variety of applications. This research utilizes quantitative methods to analyze the outcome of two bone tissue engineering studies. In an *in vivo* study, the use of Negative Pressure Wound Therapy (NPWT) in combination with stem cell-loaded scaffolds was investigated for the repair of large bone defects. Quantitative histological analysis was performed by determining both the percentage of cells proliferating (BrdU), as well as cells expressing bone-specific markers of alkaline phosphatase (ALP) in the defect. Total cell number in the defect was also determined by nuclear staining (DAPI). The results at week 1 indicated that the NPWT significantly increased cell numbers – compared to the non-treated control samples – within the defect. As a result, a direct correlation could be attributed between the use of NPWT and increased bone formation.

In a second study, tissue engineered scaffolds were evaluated for the cell adhesion and growth of mesenchymal stem cells (MSCs) and breast cancer cells (BCCs). These scaffolds were investigated for use as a potential *in vitro* model to examine breast cancer cell dormancy in the bone/bone marrow microenvironment. Fibrous scaffolds, consisting of poly-ε-caprolactone (PCL), tricalcium phosphate (β-TCP), or hydroxyapatite (HA), were fabricated using electrospinning techniques. The β-TCP and HA components are soluble and stable forms of calcium phosphate respectively, and closely mimic the

physiochemical properties of bone during active bone remodeling. Quantitative image analysis was performed using scanning electron microscopy images to determine fiber morphology, fiber diameter, and the degree of fiber alignment. These scaffolds consisted of either random or aligned fibers. Observations utilizing confocal microscopy identified MSC and BCC attached to the materials, and MSCs elongated along the aligned fibers. PicoGreen proliferation assay determined that all scaffolds supported the growth of MSCs over a two week period. The results demonstrate that the fibrous scaffolds may be a suitable three-dimensional substrate to examine BCC and MSC interaction. In summary, this thesis demonstrates the successful use of quantitative analyses in the characterization and outcome of two bone tissue engineering applications.

ANALYSIS OF TISSUE ENGINEERING STRATEGIES
FOR BONE-RELATED APPLICATIONS

by
Timothy Buirkle

A Thesis
Submitted to the Faculty of
New Jersey Institute of Technology
in Partial Fulfillment of the Requirements for the Degree of
Master of Science in Biomedical Engineering

Department of Biomedical Engineering

May 2012

Blank Page

APPROVAL PAGE

**ANALYSIS OF TISSUE ENGINEERING STRATEGIES
FOR BONE-RELATED APPLICATIONS**

Timothy Buirkle

Dr. Treena Livingston Arinzeh, Thesis Advisor   Date
Professor of Biomedical Engineering, NJIT

Dr. George Collins, Committee Member   Date
Research Professor of Biomedical Engineering, NJIT

Dr. Cheul H. Cho, Committee Member   Date
Assistant Professor of Biomedical Engineering, NJIT

Dr. Pranela Rameshwar, Committee Member   Date
Professor of Medicine-Hematology/Oncology, UMDNJ – New Jersey Medical School

BIOGRAPHICAL SKETCH

Author: Timothy Buirkle

Degree: Master of Science

Date: May 2012

Undergraduate and Graduate Education:

- Master of Science in Biomedical Engineering,
  New Jersey Institute of Technology, Newark, NJ, 2012

- Bachelor of Science in Bioengineering,
  Lehigh University, Bethlehem, PA, 2010

Major: Biomedical Engineering

PHILIPPIANS 4:13

ACKNOWLEDGMENT

Foremost, I would like to acknowledge Dr. Treena L. Arinzeh for taking me on as a member of her laboratory research team. Her expertise and valued insight really helped to guide me through my research. She was the main influence in each step I took through my experiments, and it was an honor to have worked with her.

I would also like to acknowledge the members of my Defense Committee: Dr. George Collins, Dr. Pranela Rameshwar, and Dr. Cheul H. Cho for their valuable contributions and suggestions in both my academic studies as well as my laboratory endeavors.

Additionally, I owe great thanks to the many members of the Tissue Engineering and Applied Biomaterials Laboratory – in particular Asya Bakhtina and Khady Guiro – who acted as in-lab mentors for my day-to-day work.

Lastly, I would like to thank my parents – Robert and Nancy Buirkle – who have provided me with nothing but complete support and guidance throughout my entire academic studies. If it wasn't for them, I would never have striven to reach the point where I am today. I also want to thank Jennifer Curran – her words of encouragement above all were the most effective when consoling me in times of intense frustration and lifting me up high when I at last achieved success.

TABLE OF CONTENTS

TABLE OF CONTENTS
(Continued)

Chapter   **Page**

LIST OF TABLES

LIST OF FIGURES

CHAPTER 1

INTRODUCTION

1.1   Tissue Engineering Applications

Tissue Engineering: an at times ambiguous term that has been partially defined by prominent researchers Langer and Vacanti as "an interdisciplinary field that applies the principles of engineering and life sciences toward the development of biological substitutes that restore, maintain, or improve tissue function or a whole organ" [1]. As engineers firstly, this definition appears to elude to the construction of biological tissues; however, expanding the term to include "understanding the principles of tissue growth"[2] allows for scientific methodology of research to be applied. Based upon these supplementary definitions, tissue engineering is not only the engineering of tissue and organs for therapeutic treatments, but also the study of the tissue development process in the body.

Regardless of the intended purpose, tissue engineering consists of three key factors: cells (the building blocks that ultimately make up any living tissue system), a three-dimensional matrix (scaffold) on which to seed the cells, and growth factors in order to induce cell proliferation and guidance towards the intended tissue type [3].

1.1.1 Treatment for Disease/Trauma

Bone tissue engineering can prove to be a vital supplementary component towards treating a variety of medical conditions for patients. Diseases such as osteosarcoma and osteoporosis are prevalent ailments affecting individuals of all ethnicities and genders. Osteoporosis alone affects approximately 40% of white women in the United States, and

1

is expected to reach annually estimated costs of $25.3 billion by 2025 [4]. In addition to disease, there are numerous trauma-related conditions such as the 6.8 million annually recorded bone fractures in the US [5]. Currently, 2.2 million bone graft procedures occur annually worldwide, with roughly 600,000 occurring in the US alone [6]. These grafts aide in the treatment of complex fractures as well as natural defects.

Bone grafts can originate from a variety sources such as autologous (patient's bone), allograft (donor bone), or a synthetic variant. As the aging population continues to grow worldwide due to technological advances in surgical procedures and increased life expectancies, the rise in reconstructive orthopaedic surgeries will as well. This increase has led to a heightened demand for bone grafts that far exceeds supply [3]. As a result, more attention and research has been placed in designing synthetic biomimetic bone grafts, which are cost efficient, osteoconductive/osteoinductive, contain mechanical properties similar to native bone, and less invasive than harvesting autologous bone. These grafts are biocompatible, and in some case enhance bone regeneration

1.1.2 Analyzing Cellular Mechanisms

Engineered bone tissues can serve an important role in studying and analyzing complex cellular mechanisms during development. Acting as biomimetic scaffolds, these tissues provide an artificial environment that simulate interactions occurring naturally within the body. As a result, researchers are able to apply histological techniques on samples as opposed to human subjects.

1.2 Three-Dimensional Scaffold Fabrication

Biomaterial 3-dimensional scaffolds are heavily replied upon in the biotechnology arena for both research and developing therapeutics. For tissue engineering, scaffolds can act as delivery systems for tissue-manipulating proteins and cells, as well as provide platforms in which to grow various cell types. Many factors need to be considered when constructing a particular scaffold, depending upon the desired tissue.   Chemical properties, surface chemistry, topography/architecture, and even the mechanical properties.

1.2.1 Electrospinning

The concept of electrospinning has existed for centuries, first conceptualized by William Gilbert in the 16th century[7]; however, it was not until the early 1990's where researchers such as Reneker and Rutledge began spinning nano-sized fibers from synthetic polymers. These advancements sparked a boom in the field of medical research, as scientists sought to utilize the electrospinning process as a scaffold fabrication approach in tissue engineering, due mainly in part to similarities in architecture [8].

A favorable aspect of electrospinning is the collection of nanofibers to create a high volume to surface area ratio, which is favorable for cell attachment. For example, at the Seoul National University in the Republic of Korea [9], researchers investigated the biological properties of nanofibrous polymer scaffolds with a significant concentration of interconnected pores (high porosity) against a solid-walled scaffold. Findings in an *in vitro* study with cultured osteoblasts revealed elevated levels of biomineralization, alkaline phosphatase (ALP), and osteoblast phenotype expression for the electrospun

scaffolds versus the solid-walled. Therefore, scaffold porosity and architecture appears to play a vital role in bone formation and osteoblast differentiation.

While inter-fiber spacing in general is a helpful component to electrospun scaffolds, the individual orientation of the nanofibers themselves may further enhance the biological properties such as the cells' adhesion [10, 11] and morphology [12], migration [13, 14], and even differentiation [15, 16]. In an experiment conducted at the Tsinghua University in Beijing, China, Dr. Wang et al. [17] examined the differential effects of aligned electrospun poly(3-hydroxybutyrate-co-3-hydroxyhexanoate) (PHBHHx) scaffolds on MSCs. Confocal microscopy revealed that most attached MSCs elongated along the fibers as opposed to random fiber samples. Transcriptome microarray results showed a significant reduction in the PPAR signaling pathway for aligned fibers, suggesting enhanced osteogenesis. RT-PCR and western blotting also confirmed osteogenic differentiation with the MSCs for the aligned scaffolds, demonstrating that fiber orientation plays a role in mediating stem cell fate.

1.2.2 Importance of Materials

Many factors must be considered in selecting an appropriate material(s) for tissue engineering scaffolds such as the mechanical/physical properties, intended purpose, degradation rates, biocompatiability, immunogenic properties, and effect on surrounding environment to name a few. Numerous types of biomaterials, which incorporated into manufacturing scaffolds designed for bone tissue engineering, can be broken down largely into two main groups: polymers and ceramics.

1.2.2.1 Polymer-Based Scaffolds.   Polymers are a chief component for many scaffolds, which have been used for a variety of tissue engineering purposes including bone, neural,

cardiac tissue regrowth. In recent years, a particular group of polymers – aliphatic polyesters – have gained large momentum in scaffold fabrication. Some of the more commonly used polyesters include poly(lactic-co-glycolic acid) (PLGA), poly(ε-caprolactone) (PCL), and poly-L-(lactic-acid) (PLLA).

Solely-based polymer scaffolds are able to provide suitable conditions for numerous tissue engineering applications such as neuronal [18-21], cardiac [22-24], and liver [25, 26]; however, many research reviews and articles point out the need for ceramic and/or composite scaffold materials for applications such as bone tissue engineering [8, 27].

1.2.2.2 The Use of Bioactive Ceramics for Scaffolds. To push beyond providing a stable support structure that can be easily manipulated to fit the desired mechanical and morphological inputs, many researchers are turning towards ceramics that exhibit bioactive properties, which work to manipulate the tissue environment *in situ*. Particularly in bone tissue engineering, ceramic components have drawn considerable attention due to their osteoinductive/osteoconductive tendencies in bone regeneration [28, 29]. Of the various ceramic materials used in bone tissue engineering, two particular ceramics are used due to their favorable biological properties.

Hydroxyapatite (HA) [$Ca_{10}(PO_4)_6(OH)_2$], considered one of the most stable forms of calcium phosphate, is a major component in bone (up to 65%). Furthermore, HA is known to be osteoinductive, and thus has been used as scaffolding in numerous 3-D tissue engineering experiments in conjunction with other components – chitosan, collagen, PLGA – which promote osteogenetic behavior in MSCs [30, 31]. In experiments by Ugo Ripamonti (University of Witwatersrand, South Africa), the

osteoinductive capabilities of porous hydroxyapatite (HA), created by hydrothermal conversion of coral, were observed *in vivo* in baboons. Histological analysis confirmed the presence of new bone formation in subjects three months post-surgical implantation. These results were attributed to not only the chemical makeup of HA, but also due to the porous morphology of the scaffold, which encouraged localized cell ingrowth [32].

β-Tricalcium phosphate (β-TCP) $[Ca_3(PO_4)_2]$ is a commonly used alternative to HA, which has been FDA approved in several bone products such as Vitoss (Orthovita), Mastergraft® (Medtronic), Chronos® (Synthes), Calciresorb® (Ceraver Osteal), and Biosorb® (SBM France) [33, 34]. In addition to its demonstrated osteoconductive properties, implanted β-TCP has a relatively high rate of degradation that allows for bone remodeling *in vivo* [35, 36].

As both β-TCP and HA have competing advantages for use in bone tissue engineering, several companies have sought products combining both components, such as Nuvasive's Formagraft® (60/40 β-TCP/HA) and Stryker's BoneSave® (80/20 β-TCP/HA) [3, 36]. In studies performed by Dr. Arinzeh et al. [37] *in vivo* mouse testing was conducted to determine the ideal ratio of HA/β-TCP. Ceramic scaffolds were constructed comprised of varying concentrations of β-TCP/HA. Histological testing revealed 80/20 β-TCP/HA scaffolds seeded with hMSCs resulted in superior rates of bone induction compared to competing compositions. Furthermore, *in vitro* osteocalcin assays confirmed elevated expression levels indicating osteogenic differentiation of hMSCs.

1.2.2.3 Combining Characteristics with Composite Scaffolds. While certain bioceramics show great osteoconductive and osteoinductive potential for bone regrowth,

when used individually they are far too brittle and fail to provide the needed structural support [29, 38]. Therefore, a focus has shifted towards the use of composite scaffolds, which consist of polymers as well as bioceramics in an effort to combine the advantages for both. While the ceramic elements proportionally increase bioactivity [39], the biodegradable synthetic polymer aims to provide elasticity and tensile strength [40]. In experiments by Lao et al. [41] at the Zhejiang University in Hangahou, China, the polymer PLGA was electrospun from a solution coupled with nanosize hydroxyapatite particles (HAp) in an effort to combine the mechanical advantages of a polymer along with the bioactive potential of ceramic. When tested *in vitro* with cultured mice MC3T3 preosteoblast cells, ALP secretion was significantly enhance by the composite scaffolds as compared to the PLGA controls. Similar results were also found utilizing a degraded polymer gelatin (a derivative of collagen) as a natural substrate with HA [42].

Several studies have indicated that the combined use of both β-TCP and HA in an 80/20 ratio for electrospinning fibrous mats offers a superior abilities to promote bone tissue formation compared to other concentrations [43, 44].

1.3   Cell and Tissue Analysis

In order to demonstrate a superiority of one material's use over another or to prove the existing benefits of a process in tissue engineer, a variety of analytical methods must be applied. Furthermore, these methods must act as tools to support the proposed theoretical claim.

1.3.1 Qualitative Analysis: Immunostainings and SEM

Immunocytochemistry is a fundamental aspect of tissue engineering research, as it applies an antibody-based method to detecting a given protein within a sample. After which, a variety of optical methods are called upon to detect. This can be very useful when trying to highlight certain cell processes (differentiation [45-47], proliferation [48, 49], viability) or the components within the extracellular matrix of a tissue sample (immunohistochemistry). These stainings can track the rate of change of a protein over time, as well as provide for comparative analysis between competing methods and techniques. Additionally, immunostainings can typically provide qualitative results in procedures utilizing epifluorescence/confocal microscopy.

Optical microscopy is a commonly used technique by researchers to provide a visual representation of the experiment results that support an experimental claim (hypothesis). When coupled with immunostainings, epifluorescence and confocal microscopy and allow for detailed high magnification imaging of cellular components to portray cell morphology and/or to demonstrate the presence of specific genes or proteins. Ordinarily, proteins that have forgone the immunostaining process will fluoresce when placed under a light-emitting diode at a particular excitation wavelength.
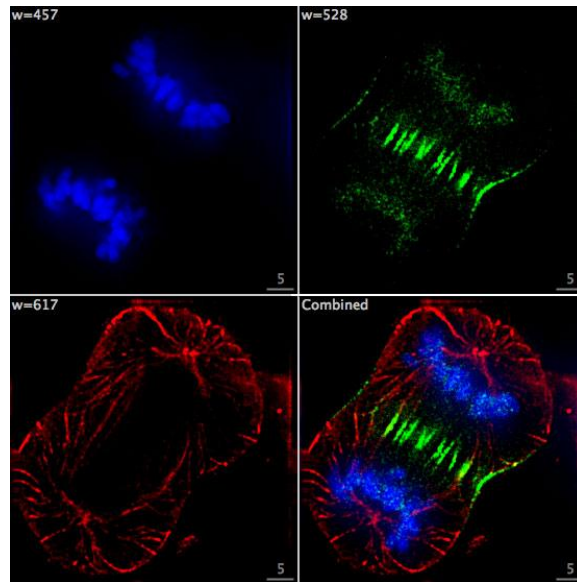
Figure 1.1 Epifluorescent image of a dividing cancer cell. DNA (blue) is stained by DAPI, protein GFP-INCENP (green), and tubulin (red). The bottom right image contains the combined rendered picture of all three images [50].

These wavelength images can then be overlaid to create a detailed image portraying several different markers. In Figure 1.1 for example, three images were captured at different wavelengths and compiled to illuminate cell structures of a human cancer cell undergoing cell division [50].

Unfortunately, there are several drawbacks of epifluorescence, one of which being a three-dimensional structure can only be in focus from one given plane. In the case of tissue engineering on scaffolds, a similar method known as confocal microscopy is used in order to obtain images with higher clarity and resolution. Using a system of lasers, multiple planed images are taken at different depths of the scaffold and then compiled to form a three-dimensional version, also known as a z-stack (Figure 1.2).
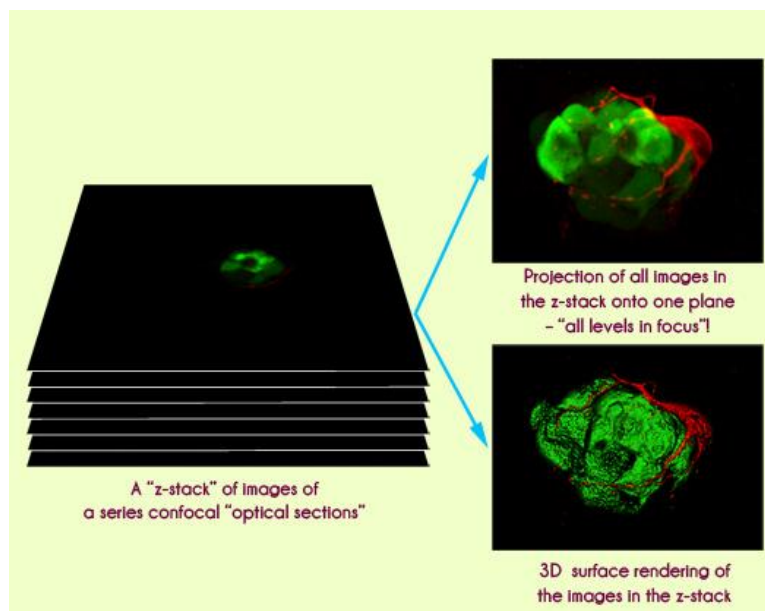
Figure 1.2: Description of the z-stack process in which a compilation of planed images can render a three-dimensional object [51].

While confocal imaging can generate a three-dimensional picture of the target proteins, it still lacks the ability to generate a clear image of the scaffold's topography; a technique called scanning electron microscopy (SEM) is used in order to accomplish this. As the name suggests, SEM directs a beam of electrons at the intended sample, registering highly magnified images with a resolution superior to optical imaging (Figure 1.3). Whether a confocal or an epifluorescence is used, the resultant image is primarily used for illustrative purposes. When comparing biomolecular processes, additional testing is typically followed in order to obtain quantitative results that provide more concrete evidence.
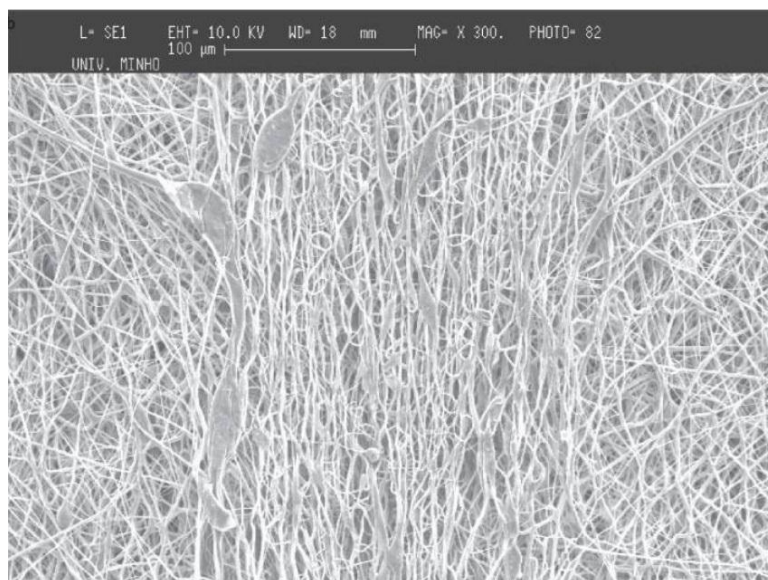
Figure 1.3 Sample SEM image taken of a PCL nanofiber scaffold [52].

1.3.2 Quantitative Analysis

Quantitative data provides a concrete objective analysis for an experiment, enabling the research team to draw conclusions more readily than through visual examination as in imaging techniques. Typically, quantitative analysis is conducted with greater ease in experiments *in vitro* since the entire sample can be analyzed as opposed to the entire subject of an *in vivo* experiment. *In vitro* studies allow for more control over variables such as the ECM components in media. For example, Polini et al. [53] at the National Nanotechnology Laboratory in Lecce, Italy utilized several assays in order to test the osteoinductive capabilities of several different scaffolds composed of combinations of PCL, HA, and β-TCP. When conducting *in vitro* testing with seeded hMSCs, quantitative proliferation assays revealed consistent growth curves over a six day period. In addition, Polini's team used semi-quantitative image analysis in determining ALP levels to denote osteogenic differentiation. The term "semi-quantitative" is appropriate in this case since ALP levels were obtained by converting the stained images to grey-scale, highlighting the region of interest (ROI) containing the visible ALP, and then recording the mean

intensity value (Figure 1.4). Therefore, when comparing levels of ALP expression among scaffold types, judgments are based upon image brightness as opposed to the actual numeric quantity of ALP.
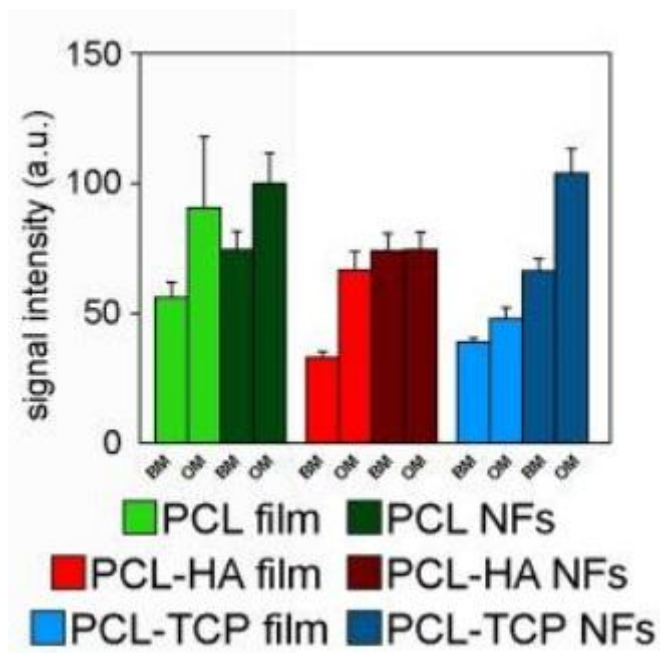
Figure 1.4 Graph of signal intensities within the ROI of ALP-stained images for various scaffold types and compositions [53].

CHAPTER 2

RESEARCH OBJECTIVES

The following research investigated and analyzed bone tissue engineering strategies for bone repair and cancer applications using various quantitative immunohistological and immunocytochemical techniques. First, several immunohistological techniques were applied to an *in vivo* model involving the use of bioactive ceramic scaffolds, mesenchymal stem cells, and vacuum assisted closure (VAC) therapy to repair a rabbit radial defect. The goal of this study was to analyze and compare experimental treatments in order to determine which strategy would prove to be the most effective. In order to analyze the contribution of the mesenchymal stem cells and other host cells in bone repair, immunostaining was performed for specific protein markers to observe cell proliferation as well as osteogenic differentiation. The purpose of this bone defect study was to determine whether the use of VAC in combination with the scaffolds and MSCs would improve repair as compared to groups without VAC therapy.

A second study investigated the bioactive properties of fabricated biomimetic bone tissue scaffolds. Previous research has denoted the benefits of fiber orientation as a means of enhancing cellular behavior. The goal of this study was to create aligned electrospun scaffolds whose components would mimic the physiochemical properties of bone. Cell attachment and cell proliferation were analyzed using immunostaining techniques. The hypothesis of this work was that the aligned fiber scaffolds would demonstrate an increased cell attachment, osteogenic differentiation, and cell viability.

CHAPTER 3

IMAGE ANALYSIS FOR IN VIVO STUDY

3.1   Experimental Set-Up

The following study provides an inside look into the utilization of tissue engineering for the purpose of developing novel medical treatments – bone regeneration in patients who have underwent orthopaedic surgery in response to trauma, reconstruction, or skeletal defects. More specifically, immunohistochemical analysis was performed for an *in vivo* preclinical trial on rabbits to test the effects of a potential treatment – vacuum-assisted closure (VAC), which is a form of negative pressure wound therapy used to aide in would closure [54, 55]. Therefore, this experiment tested the effectiveness of VAC therapy in conjunction with orthopedic surgical techniques.

Prior to experiments, the rabbits were divided into two main groups: those receiving NPWT treatment, and those that did not undergo therapy. In order to evaluate the potential use for NPWT conjointly in implant/graft surgeries, the two main groups were each divided into the following three subgroups: subjects that received an implant at the defect site, subjects that received an implant seeded with marrow-derived rabbit mesenchymal stem cells (MSCs), and subjects who had no implant (control). Lastly, each subgroup was divided further into two post-surgery evaluation groups – Week 1 and Week 8 - in order to track both the short and long-term effects of the given treatments. Each specific group had a sample size of four to allow for statistical significance.

In the surgical procedures, New Zealand White rabbits were each given a 1.5 cm segmental defect along the radius. The corresponding groups then received varying combinations of treatment involving NPWT and implantation of the synthetic porous

graft (60/40 w/t hydroxyapatite/beta-tricalcium phosphate) with or without seeded MSCs. Including the main treatment (VAC), secondary treatments (implant or MSC-implant), and controls, there were a total of six treatment groups. Each rabbit subject was then sacrificed according to its designated evaluation group and then prepared for histomorphometry and immunohistochemical analysis.

3.2   Materials and Methods

3.2.1 Cellular Protein Stainings

In order to demonstrate and compare the rates of bone regrowth for the rabbit subjects, both the cell proliferation and osteogenic differentiation percentages needed to be calculated. In order to achieve this, three immunostainings were performed. The synthetic nucleoside 5-bromo-2'-deoxyuridine (BrdU) (Sigma) was chosen as an immunostaining to highlight proliferating cells based upon previous study successes [48, 49]. A solution containing Fast Red TR/Naphthol (FR/NAP) (Sigma-Alderich) was added in which bound to alkaline phosphate (ALP) that was present in the defect sites during osteogenesis. Lastly, DAPI – a nuclear stain for all cell types – was used to calculate the total cell numbers in a sample for the purpose of calculating the proliferation and differentiation percentages.

In preparation for staining, all histological samples were first removed from the freezer and hydrated in a 400µl solution of Dulbecco's Phosphate Buffered Saline (PBS) (GIBCO) for twenty minutes at room temperature (RT). After decanting the PBS and carefully wiping the sides of the slide, a hydrophobic barrier was applied around the edges of the sample using a Super PAP Pen Liquid Blocker (Ted Pella) in order to reduce

the required solution volumes per sample and to prevent spilling during storage and imaging. For all staining procedure steps, samples were incubated at RT unless otherwise specified.

3.2.1.1 ALP Staining for Differentiation. Before staining, a solution of AP Buffer was prepared, consisting of 100mM tris(hydroxymethyl)aminomethane hydrochloride (Tris-HCl), 100mM sodium chloride (NaCl) (Sigma), and 5mM magnesium chloride (MgCl2) in distilled water (dH$_2$O). Histological samples were decanted of PBS, wiped clean (Kimberly-Clark Kimwipes), and soaked in 400µL AP Buffer for five minutes to better prepare the tissues for staining. Next, the AP Buffer is decanted, and the slide wiped dry. Then, 400µL of 1:100 FR/NAP in AP Buffer were added for 12-15 minutes. This step was performed in a minimal light environment to prevent overexposure of the Fast Red TR. After a maximum of 15 minutes in which ALP was visibly present in red, the slides were rinse with 10mL of PBS, at which point the ALP staining was complete.

3.2.1.2 BrdU Immunostaining for Proliferation. When immunostaining for cell proliferation, monoclonal anti-BrdU was used in conjunction with a secondary fluorescent antibody – goat anti-mouse FITC conjugate (FITC) (Abcam). Anti-BrdU formed attachments to BrdU, which would replace thymidine nucleosides in newly synthesized DNA strands during a cell's S-Phase. The secondary antibody, FITC, would attach to anti-BrdU and highlight proliferating cells by fluorescing at 528nm (green).

Fixed samples that were already hydrated in PBS were decanted and wiped drip. A 400µL solution – 0.1% Pepsin (ACROS) in (0.1 molar concentration (M) HCl in PBS) – was first applied. The samples were placed into an Isotemp 120 (Fisher Scientific) humidified chamber at a temperature of 37°C for a 50 minute incubation period. The

slides were then decanted and wiped again, and set in a 400μL 2M of HCl in dH$_2$O. Thirty minutes of incubation in the Isotemp allowed just enough time for the HCl to permeablize the cells' membrane and denature the DNA, but without damaging the cells to the extent of being unrecognizable. Afterwards, the slides were thoroughly rinsed with 50mL of PBS and checked for pH levels ~7.0 (neutral acidity level for water). If the pH level was six or lower, then the rinse process was repeated. Prior to antibody treatment, the cells were blocked using a solution of 5% normal goat serum (NGS) in (1% bovine serum albumin (BSA) in PBS) for one hour. The samples were then ready to begin antibody exposure.

The primary antibody, monoclonal anti-BrdU (Sigma-Alderich), was mixed 1:1,000 in a solution of 1% NGS in (1% BSA in PBS). Following decantation and wiping, 400μL of solution were applied, and samples were placed in a humidified chamber to store overnight at 4°C. On day 2 of the staining, slides were removed from the chamber and soaked three times in 400μL PBS for ten minutes. After decanting and wiping, the secondary antibody FITC was mixed 1:500 in a solution identical to anti-BrdU and applied for one hour in darkness. Lastly, the slides were rinsed three times in PBS for five minutes each, and stored in 500μL PBS in the humidified chamber at 4°C until needed for analysis.

3.2.1.3 DAPI Nuclear Stain for Cell Population. All slides underwent a DAPI stain just prior to imaging in order to visualize the total present cells per sampling. Initially, 200μL of PBS were applied, followed by two drops of SlowFade® Gold antifade reagent with DAPI (Invitrogen). The solution was then decanted, the slide was wiped clean, and 300μL of PBS were added.

3.2.2 Fluorescence Microscopy

After the samples were appropriately stained, fluorescence microscopy was run using NIS-Elements AR 3.2 software (Nikon). Three fluorescent lightings were used at 10x magnification for these experiments: red (ALP), green (FITC/BrdU), and blue (DAPI). Samples for week 1 were imaged for all three components (ALP, proliferation, total cell population); however, week 8 was only imaged for ALP and total cells (DAPI) since bone regeneration was complete, ceasing cell proliferation.

For each subject, two adjacently sliced samples were analyzed in which one sample slide was stained and imaged for ALP and BrdU (depending on sample), and the other slide for DAPI. Fluorescent images were recorded at identical sample locations in order to later overlay the two for ALP analysis (section 3.3.1). Images then underwent denoising to remove any recorded background interference (Figure 3.1).
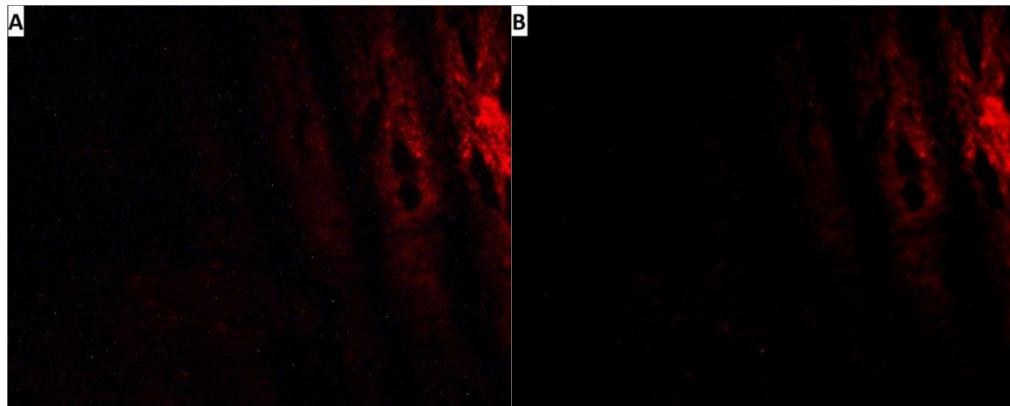
Figure 3.1 Red-fluorescent image of alkaline phosphatase for week 1 rabbit subject; image is first captured (A) and then filtered using image denoising (B) in order to provide more contrast, and perform analysis more efficiently.

In rabbit subjects that only had the defect (no implant and/or MSCs), the following six images were taken: four images from the corners of the bone/defect site, and two images from the center of the defect (Figure 3.2). This process allowed for the comparison of tissue regrowth from several areas in order to ensure a uniform rate

throughout the sample. Additionally, this method provided consistency and helped to remove human error in the form of arbitration.
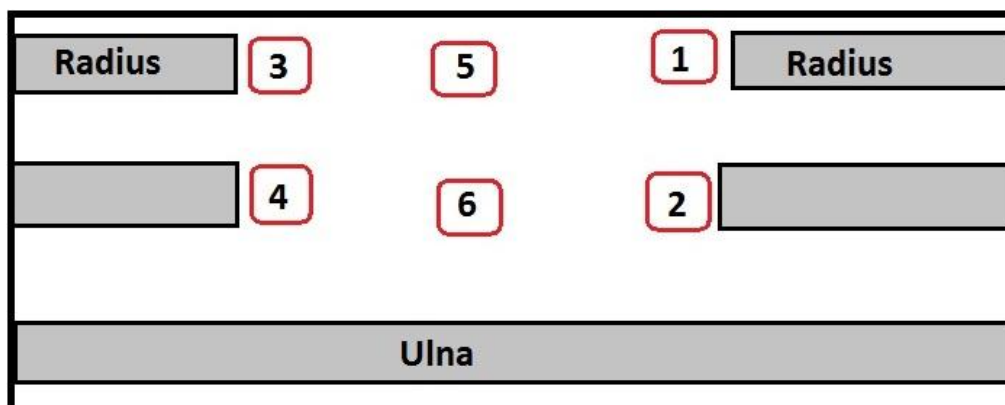
Figure 3.2 Schematic of images taken from the defect area.

3.2.2.1 Object Count for Cell Sample Population.   For determining the number of DAPI-stained cells and proliferating BrdU-stained cells, the Object Count function was used, which registered cell presence based upon specified morphology (circularity) and fluorescent intensity thresholds (Figure 3.3).
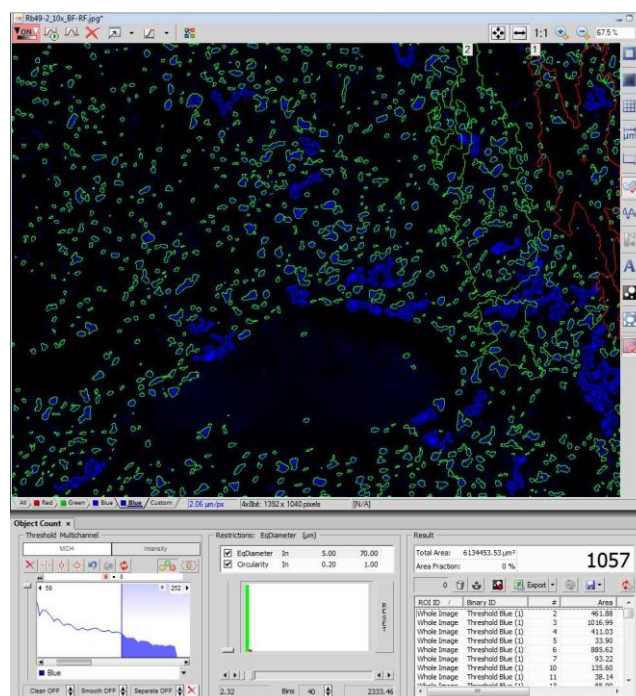
Figure 3.3 Cell Count feature for determining sample populations; features picked up in the intensity threshold range are highlighted in blue; features recognized as cells are outlined in green.

3.2.2.2 Regions of Interest (ROIs) for ALP Analysis. In order to determine estimated levels of ALP in samples for comparison, percentages were calculated based upon cell counts. First, one or more ROIs were created using the autodetect feature in order to (Figure 3.4A) establish the areas of ALP in which to count the cells present. Next, the red-filtered samples were overlaid with the blue-filtered DAPI images, and a cell count was performed for cells within the ROI (Figure 3.4B). This was then compared against sample population count (section 3.2.2.1) in order to get a percentage of ALP expression.
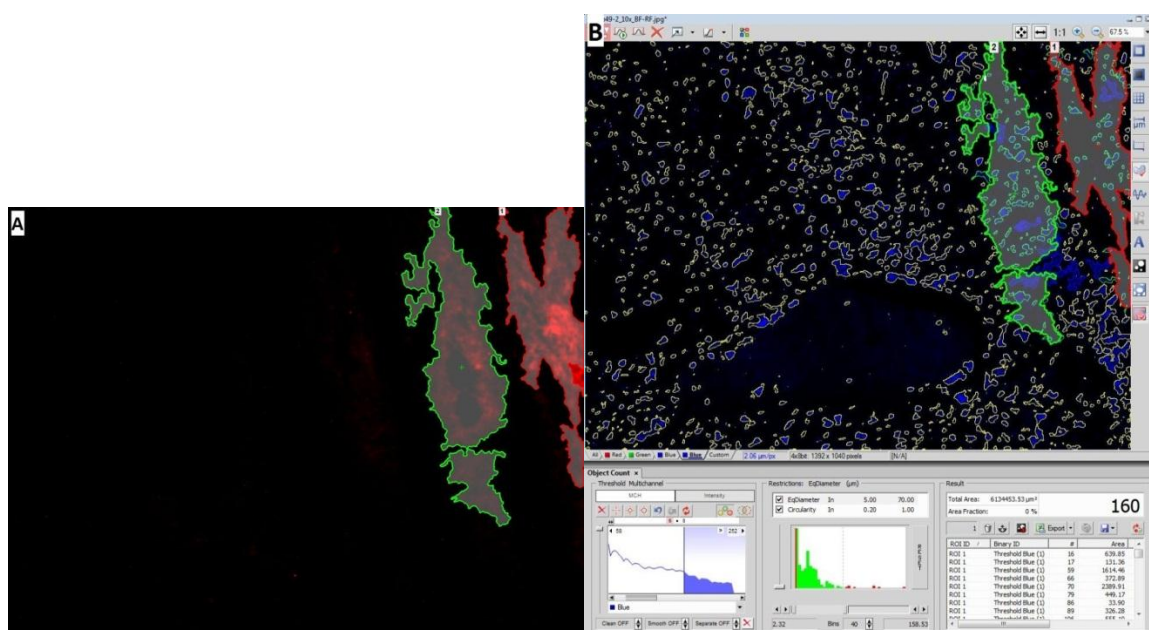
Figure 3.4 Determining the levels of ALP expression by highlighting ROIs (A) and counting the number of cells present within the selected area (B); objects recognized by the Object Count are highlighted (blue), depicting objects counted (green outline) and not counted (yellow outline).

3.2.3 Statistical Analysis

All quantitative data underwent statistical evaluation in order to determine the presence any significant differences. More specifically, statistical inference for independent populations via t-testing was performed with the level of significance, $p < 0.05$.

3.3   Results and Discussion

The following sets of data and analysis are a compilation of the results of the eight week experiment involving the defective rabbit radius, which underwent surgical treatment. The osteoconductive as well as proliferative capabilities are examined in the expression of ALP and BrdU, respectively.

3.3.1 Osteogenic Differentiation: ALP Expression

Each subject was imaged for both DAPI (blue) and ALP (red) at 10x magnification. These images were then overlaid to demonstrate when the ALP was expressed in relation to the viable DAPI-stained cells. Unlike the cell nuclei which can be easily distinguished from one another, the visualization of ALP had a degree of arbitration. To counteract this, the background interference was used as a guide to determine the true levels of ALP picked up by the light emitting diode. For example, in Figure 3.6B the intensity of the red spectrum was raised to the point of visualizing the background interference in order to show that no ALP was present within the sample. The contrary can be seen in figure 3.5B, where the expression of ALP is visible despite low levels of background interference.

The DAPI and ALP$^+$ cell counts were recorded for all images, the percentage of ALP expression was calculated (adjacent to bone, center of defect, pore site, canal) in each sample group (n=4), and then the values were averaged for comparative analysis (Table 3.1). Fluorescent imaging and qualitative analysis showed that for week 1 subjects the expression of ALP was negligible at both the center of the bone defect and in the canal of the implant scaffold. Defect only subjects receiving the VAC treatment also appeared to have higher levels of ALP, although not enough for statistical significance.
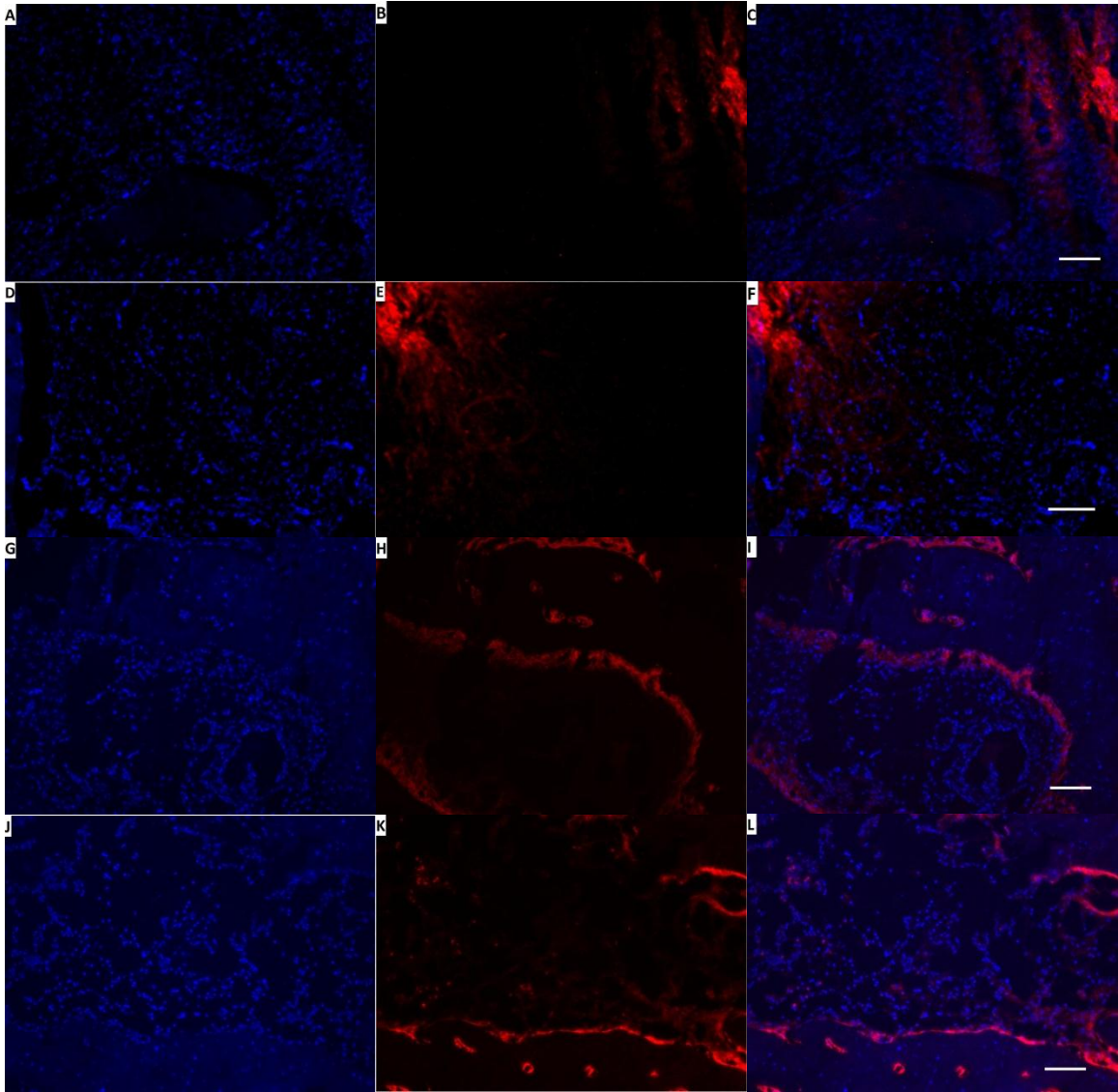
Figure 3.5 Fluorescence microscopy for rabbit subjects receiving no implant (defect only). Week 1 rabbits were divided into those receiving VAC (D-F) and those without VAC (A-C). Week 8 subjects were also grouped accordingly with VAC (J-L) and without VAC (G-I). For each image, ALP (red), excreted from osteogenic cells into the ECM, appear as cloud-like formations; the DAPI (blue) represents the individual nucleus of each cell present.
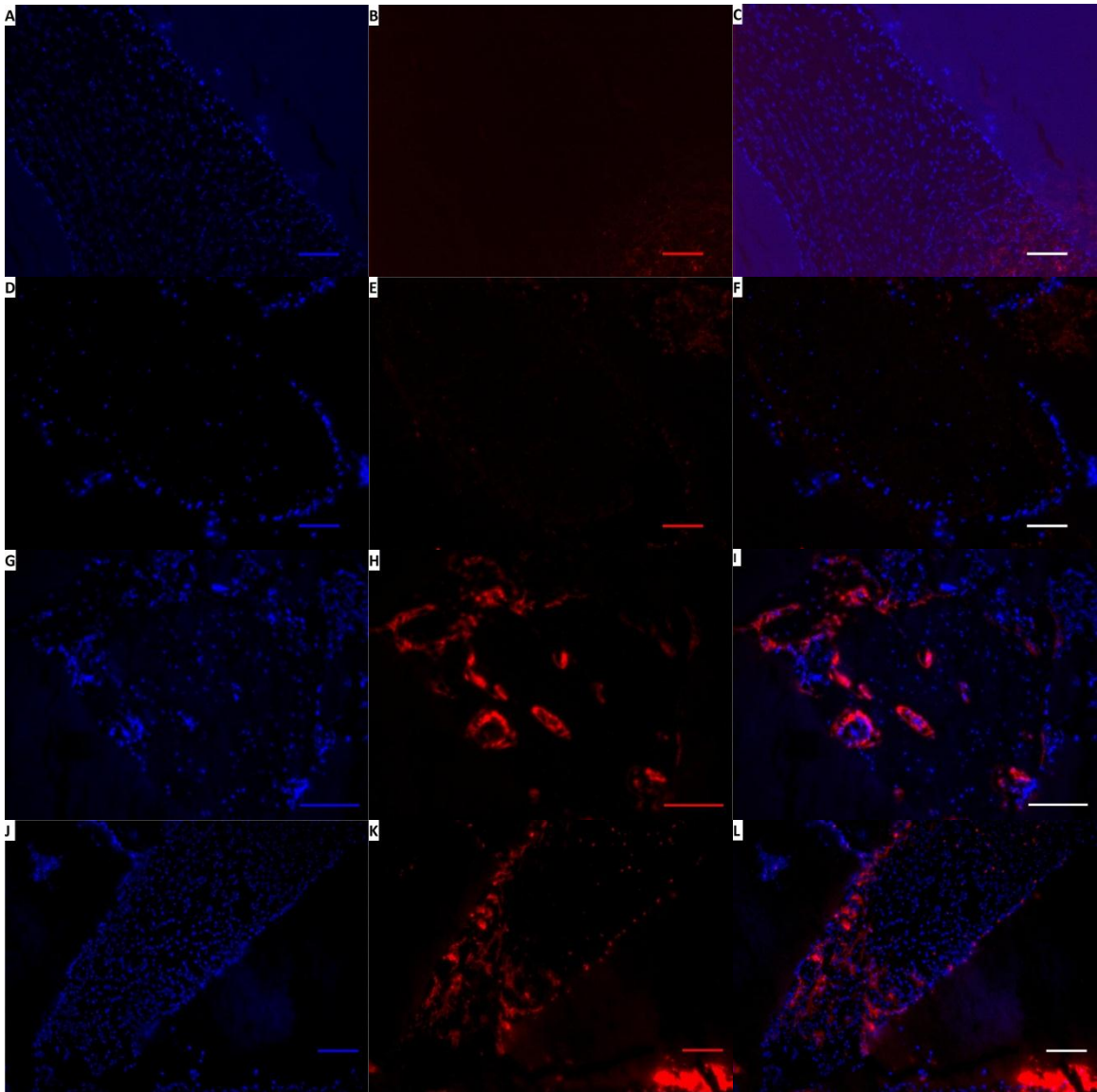
Figure 3.6 Fluorescence microscopy for rabbit subjects receiving an implant. Week 1 rabbits were divided into those receiving VAC (D-F) and those without VAC (A-C). Week 8 subjects were also grouped accordingly with VAC (J-L) and without VAC (G-I). For each image, ALP (red), excreted from osteogenic cells into the ECM, appear as cloud-like formations; the DAPI (blue) represents the individual nucleus of each cell present.
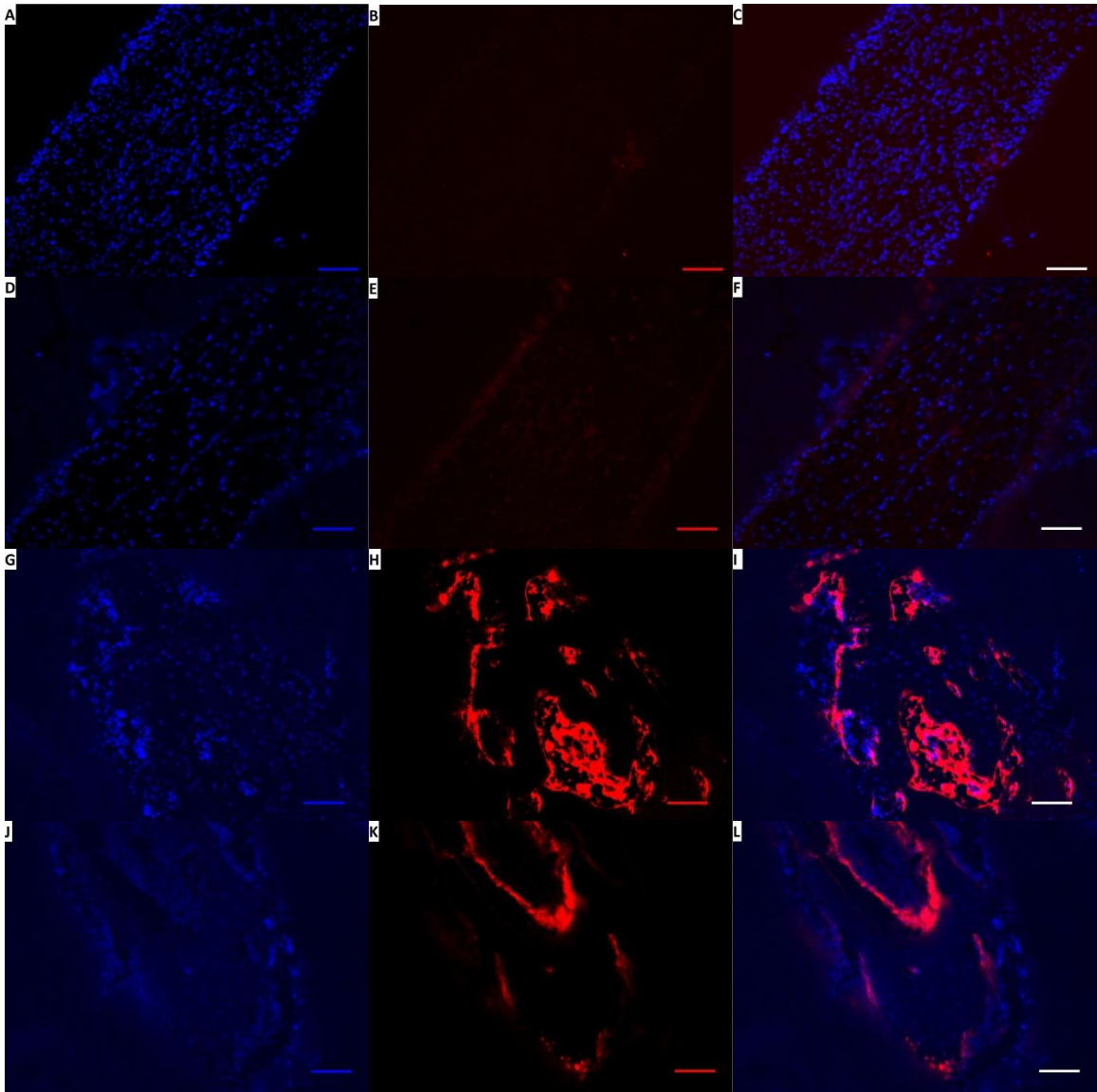
Figure 3.7 Fluorescence microscopy for rabbit subjects receiving MSC-loaded implant. Week 1 rabbits were divided into those receiving VAC (D-F) and those without VAC (A-C). Week 8 subjects were also grouped accordingly with VAC (J-L) and without VAC (G-I). For each image, ALP (red), excreted from osteogenic cells into the ECM, appear as cloud-like formations; the DAPI (blue) represents the individual nucleus of each cell present.

Table 3.1 Average ALP Data for All Rabbit Groups

Duration/Treatment	VAC	Image Location	% ALP
Week 1 Defect Only	No VAC	All Locations	4.45±3.14
		Adjacent to Bone	6.68±4.71
		Center of Defect	0.00±0.00
	With VAC	All Locations	7.60±6.32
		Adjacent to Bone	11.39±9.49
		Center of Defect	0.00±0.00
Week 8 Defect Only	No VAC	All Locations	22.90±5.94
		Adjacent to Bone	34.35±8.93
		Center of Defect	0.00±0.00
	With VAC	All Locations	18.39±4.57
		Adjacent to Bone	24.75±5.55
		Center of Defect	5.66±6.31
Week 1 Implant	No VAC	All Locations	3.15±3.57
		Pore Site	4.20±4.76
		Implant Canal	0.00±0.00
	With VAC	All Locations	1.24±0.76
		Pore Site	1.65±1.01
		Implant Canal	0.00±0.00
Week 8 Implant	No VAC	All Locations	26.84±7.08
		Pore Site	25.99±8.45
		Implant Canal	29.38±4.52
	With VAC	All Locations	24.86±14.12
		Pore Site	26.52±14.51
		Implant Canal	19.89±13.73
Week 1 Implant + MSC	*No VAC	All Locations	0.00±0.00
		Pore Site	0.00±0.00
		Implant Canal	0.00±0.00
	With VAC	All Locations	0.00±0.00
		Pore Site	0.00±0.00
		Implant Canal	0.00±0.00
Week 8 Implant + MSC	No VAC	All Locations	9.19±8.10
		Pore Site	8.03±8.88
		Implant Canal	12.12±8.61
	With VAC	All Locations	10.34±3.75
		Pore Site	9.71±4.25
		Implant Canal	12.23±9.83

Values = mean ± standard deviation; *Week 1 Implant-MSC groups had no significant ALP expression in cells.

Subjects receiving the MSC-loaded implant showed no significant levels of ALP expression at all locations during week 1 (the very select few images which contained trace amounts of ALP were ruled statistical outliers and discounted from the results). Theses finding were verified visually by Figure 3.7, in confocal images B and E, which also show no visible ALP in the pores or canal. At week 8, ALP levels for MSC-loaded were still recorded at relatively lower levels than for defect or implant only. Unfortunately, these was a considerable degree of variability overall between samples in each group, which created high levels of variance (large standard deviations). As a result, statistical significance between treatments over time was difficult to determine.

3.3.2 Proliferation: BrdU Expression

Each rabbit sample designated for week 1 was stained with BrdU, imaged using fluorescent microscopy (green), and analyzed using Object Count for proliferating cell numbers. Each analyzed image group was then compared to determine any significant differences in tissue regrowth (proliferation). Figure 3.8 displays a BrdU fluorescent image for each week 1 rabbit experimental group. Sample groups receiving no VAC treatment (left) were compared against those with VAC (right). Additionally, the treatments of defect only (A,B), implant (C,D), and MSC-loaded implant (E,F) were cross-analyzed to determine any variations in the rate of tissue regrowth.

For rabbits groups containing implants (C-F), six images were taken at pore sites and two images from the implant canal. Non-implant groups (A,B) had four images taken adjacent to the host's bone as well as two images at the defect's center. At pore sites, the proliferating cells can be seen at the edges and center, indicating tissue regrowth into the porous implant material.

In samples that received VAC therapy, there was a statistically significant difference in the percentage of BrdU-stained cells, indicating high rates of proliferation compared to controlled samples not receiving the therapy ($p<0.05$) (Table 3.2). These differences are observable at both the locations adjacent to the bone as well as at the center of the defect. Overall, BrdU levels appear to be constant through their respective samples, regardless of where the image was taken. This demonstrates a uniform level of tissue regrowth for the sample depending upon the given treatment or therapy.

Table 3.2 Percentage of BrdU Positive Cells for All Week 1 Samples

		Control	VAC
Defect Only	All Locations	11.56±4.15	*20.81±4.53
	Adjacent to Bone	11.22±3.57	*20.41±2.52
	Center of Defect	12.12±5.03	21.61±11.06
Implant	All Locations	24.59±14.28	15.57±5.02
	Pore Sites	24.81±15.29	16.48±3.82
	Canal	23.93±16.81	12.87±11.29
Implant + MSCs	All Locations	26.32±5.67	37.91±18.07
	Pore Sites	25.67±3.21	37.07±17.53
	Canal	28.29±13.46	40.52±19.84

Value = average ± standard deviation; *Percentage BrdU$^+$ cells for defect only samples with VAC were higher than control group without VAC ($p<0.05$).
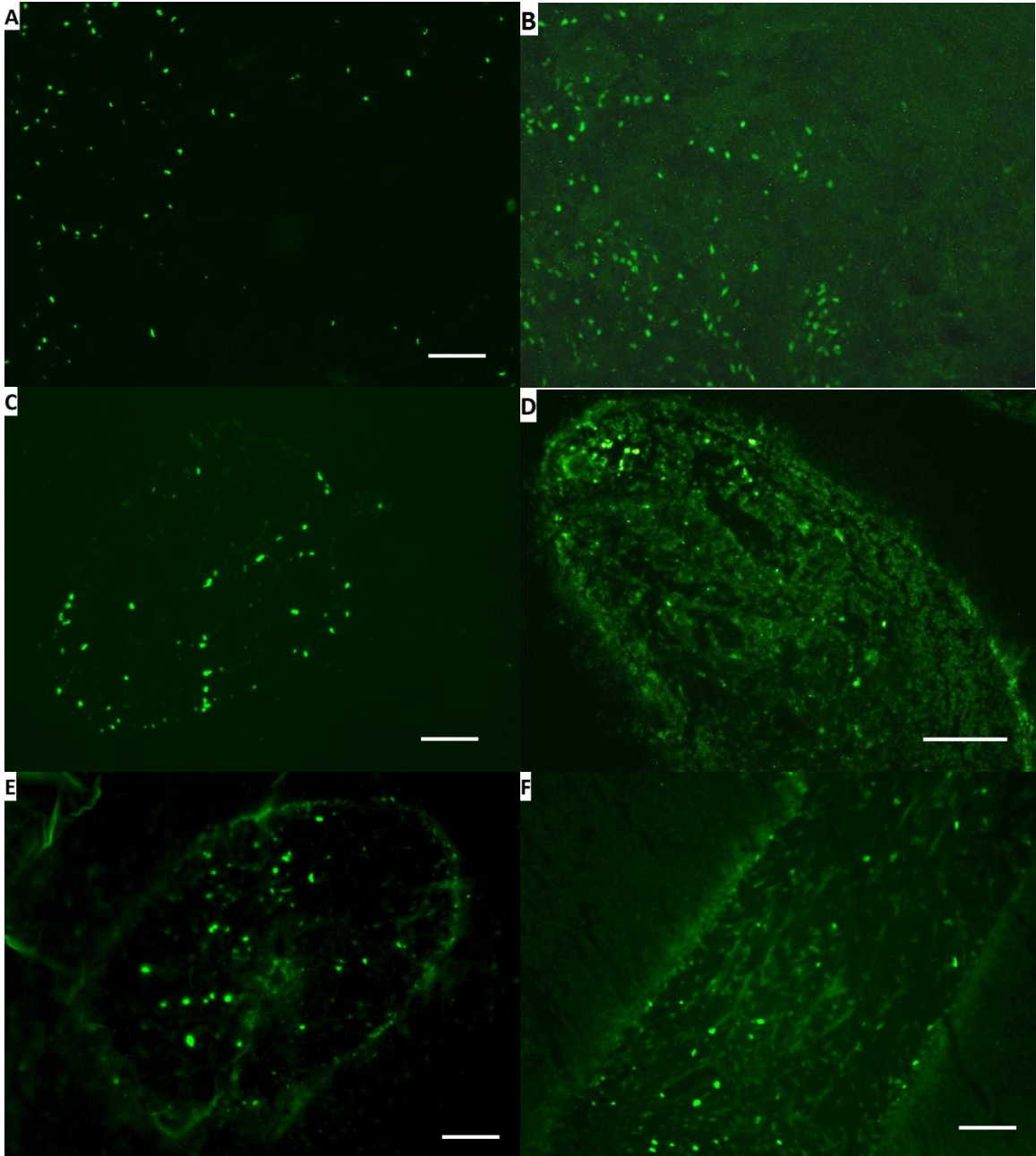
Figure 3.8 Green fluorescent microscopy images for the following Week 1, BrdU-stained proliferating cells: defect only samples (A,B), implant (C,D), and MSC-loaded implant (E,F) receiving either no additional treatment or VAC therapy, respectively.

CHAPTER 4

SCAFFOLD DEVELOPMENT AND ANALYSIS FOR IN VITRO STUDY

4.1   Experimental Set-Up

Previous research has indicated that the cellular mechanisms relating to breast cancer remission may be linked to mesenchymal stem cells (MSCs) [56]. MSCs are believed to form intercellular connections via gap junctions with BCCs [57], facilitate their migration into the bone marrow using chemotaxis [58], and may even provide an exchange of nutrients to maintain BCC viability. Additionally, MSCs immunogenic properties may play a factor in preventing the body from attacking these dormant BCCs [59, 60].

This experiment called for a comparative *in vitro* study in which BCC-lines (active and dormant) were co-cultured with hMSCs on simulated bone tissue in order to better simulate the environmental conditions in the body. Bioactive scaffolds were electrospun using ceramic components natural found in bone such as hydroxyapatite (HA) and tricalcium phosphate (β-TCP). Synthetic polymer (PCL) was also chosen to decrease the scaffold's brittleness and promote more favorable mechanical properties.

BCCs (cell line: MDA-MB-231) were genetically modified to express OCT-4 green fluorescent protein (GFP) when in states of dormancy. As a result, two comparable cancer cell lines were created when sorted – dormant BCCs with high levels of expression (OCT4-Hi) and active aggressive BCCs with low levels (OCT4-Lo).

These experiments provided the necessary background work in order to conduct a thorough study investigating the intercellular connections between these cell types. To assure these results and methods are sound with minimal outlying variables, testing needs

29

to first be performed on a variety of components such as the scaffolds, analytical components used in immunoassays, and cell-to-scaffold attachment properties.

4.1.1 BCC Attachment and Morphology Study

The first preliminary experiment dealt with BCC attachment to the various scaffold fibers. While previous studies had shown success in seeding the BCCs onto biomimetic scaffolds, testing needed to prove that these cells were capable of attaching to theses specific scaffold types and could easily be distinguishable under confocal microscopy.

For this to be successful, BCCs with both high and low expressions levels of OCT-4 were each chosen in order to portray quiescent and active cancer cells respectively. Each cell type was then seeded onto four different random fiber scaffolds at seeding density of 1000 cells/sample: PCL, PCL/HA, PCL/β-TCP, and aligned PCL (Table 4.1). Only four scaffolds were chosen for the experiment due to both the cost and availability of the specific BCC types. For each BCC-scaffold sample, there were three time duration subgroups at days 1, 2, and 4. Lastly, each subgroup was given a sample size of 2, in event of there being a discounted sample due to unforeseen abnormalities.

Table 4.1 Plate Layout for BCC Attachment and Morphology Study

	PCL			PCL/HA			PCL/β-TCP			Aligned PCL		
	1	**2**	**3**	**4**	**5**	**6**	**7**	**8**	**9**	**10**	**11**	**12**
A	Lo	Hi		Lo	Hi		Lo	Hi		Lo	Hi	
B	Lo	Hi		Lo	Hi		Lo	Hi		Lo	Hi	
C												
D												
E	Lo	Hi										
F	Lo	Hi										
G												
H												

*This plate layout is representative of one time point only

Immunostainings were carried out using DAPI as a nuclear stain, as well as rhodamine phalloidin to highlight actin formation in the cytoplasm and examine cell morphology. All cell samples were then examined for expression of GFP, DAPI, and actin via confocal microscopy, and images were captured using NIS-Elements AR software (Nikon).

4.1.2 Scaffold-MSC Viability and Morphology Study

This study investigated the bioactive capabilities of aligned fiber scaffolds towards human mesenchymal stem cells (MSCs) in regards to cell attachment, morphology, and proliferative viability. MSCs were seeded onto scaffolds of four separate compositions (see section 4.1.3) with both aligned and random fiber orientations (eight total mat types). Upon seeding at 1000 cells/sample in general media, samples were analyzed at days 1, 4, 7, and 14 in order to track the scaffold-cell interactions over a two-week period. The MSC morphology was captured via confocal images of nuclear and actin immunostainings. Quant-iT™ PicoGreen® dsDNA Reagent quantitatively determined the cell population for each individual sample.

4.2   Materials and Methods

4.2.1 Scaffold Fabrication

Throughout the BCC-MSC study, two different fiber configurations were examined: random fiber mats (RM) and aligned fiber mats (AL). For each fiber configuration, four choices of materials were chosen due to their proven results in experimentation and demonstrated superior mechanical properties in comparison to other biomaterials. First, a synthetic degradable polymer material was chosen: 15% w/w PCL dissolved in MC. Two

other mats were composites, comprised of 10% w/w PCL in MC solution in 30w/w of either HA or β-TCP. Lastly, a fourth composite mat was investigated, consisting of 10% w/w PCL in MC solution in a 30% w/w 80/20 blend of β-TCP and HA respectively.

4.2.1.1 Solution Preparation. Prior to electrospinning, each solution was prepared using Methylene Chloride (MC) as a solvent, mixed with the desired concentrations of PCL (Alderich), HA (Berkeley Advanced Biomaterials), β-TCP that act as the solutes. Prior to adding the ingredients, the vial and stirrer were first rinsed in a MC bath to ensure there is no residue present from previous trials. The individual solutes were then weighed out on the electric scale (Ohaus Corporation, USA) based upon desired concentration and volume of solution – for these experiments, all solutions had a mass of 10 grams. After pipetting the calculated amount of MC, the open solution was placed on the magnetic stirring plate (Corning). At this point, the PCL beads were then added to the solution while stirring; this ensured that the magnetic stirrer did not become lodged at any point. The lid was promptly screwed on tightly afterwards to prevent the fast-evaporating MC from venting and thickening the solution. After roughly one hour of mixing, solutions prepared for pure PCL mats were deemed ready for electrospinning after 2 minutes under a digital sonicator (Branson Ultrasonic Corp.) to relieve trapped air and break apart any remaining particles. For designing composite scaffolds containing ceramic components, desired amounts of HA and β-TCP were weighed out on the electric scale, slowly added to the dissolved PCL-MC solution, mixed for two hours, and then sonicated for 2 minutes before being electrospun. The % w/w of PCL in composites was reduced (from 15% to 10%) in order to maintain a low enough viscosity to prevent clogging in the needle when spinning.

4.2.1.1 Random Mat Electrospinning.   Each prepared solution was loaded into a either a 10 or 20mL plastic syringe (BD), equipped with either a 12 or 20 gauge needle for polymer and composite solutions respectively (Table 4.2). For scaffolds composed only of polymer PCL, a closed environmental chamber was used in order to manipulate the humidity to the necessary levels needed for spinning (Figure 4.1) Composite-type scaffolds required an open chamber set-up in which the solution was subject to the natural temperature and humidity levels, which were recorded at the commencement of the electrospinning process. As a result, composite scaffolds could only be constructed during midday under fair-weather conditions in which humidity levels were significantly lower.

Table 4.2 Electrospinning Parameters for All Scaffold Mat Types

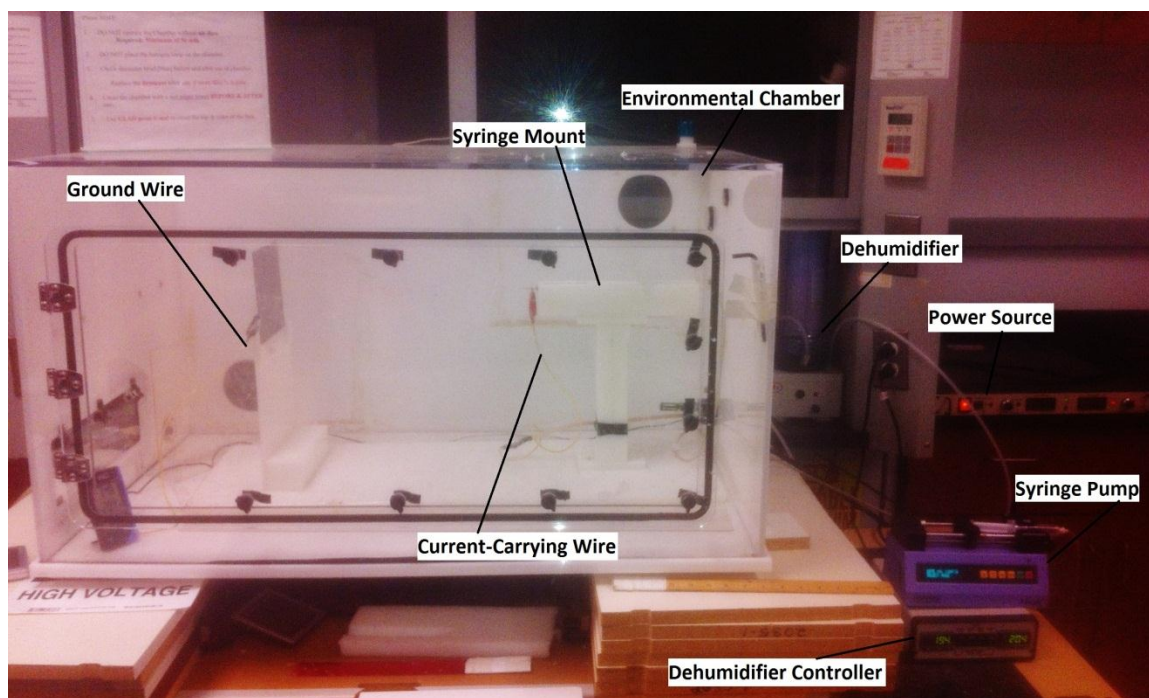| Fiber Type	Components	Needle Gauge	Collector Distance (cm)	Voltage (V)	Flow Rate (mL/hr)	Machine
Random	PCL	12	40	20kV	7	3rd Floor, Controlled
	PCL + Ceramic	20	40	20kV	3	2nd Floor, Open
Aligned	PCL	12	20	20kV	7	3rd Floor, Controlled
	PCL + Ceramic	20	20	20kV	3	2nd Floor, Open

Figure 4.1 Diagram of environmental chamber for PCL electrospinning process.

A Harvard Apparatus syringe pump controlled the flow rate of the solution, which was charged by a current carrying electrode connected to a 20kV DC power source (GAMMA High Voltage Research). A grounded 8"x8" collecting aluminum plate, located 40cm from the needle tip, accumulated the randomly oriented fiber strands as they shot from the syringe (Figure 4.2).
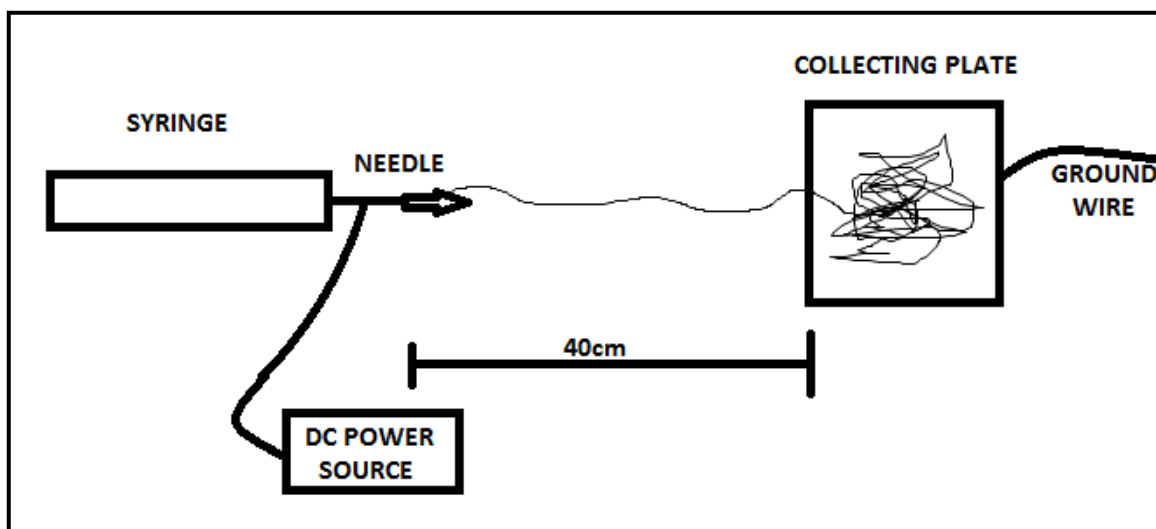
Figure 4.2 Set-up for random mat electrospinning.

4.2.1.2 Aligned Mat Electrospinning.   For aligned fiber spinning, the majority of parameters were duplicated from the random mat protocol, such as voltage, needle gauge, and flow rate (Table 4.2). In this case, the distance was shortened to 20cm as opposed to 40cm in order to increase fiber accumulation efficiency. The collecting plate was replaced with a foil-covered rotating drum (rotating diameter = cm) (Figure 4.3), kept at a high RPM of 1,000-1,300 using a Nova-Strobe series stroboscope (Monarch Instrument); lower RPMs resulted in unaligned fiber mats. Since the surface area was significantly larger for the drum (A = cm^2), 2-3 batches of solution were used for each spin in order to obtain an aligned mat of relative thickness compared to random mats.
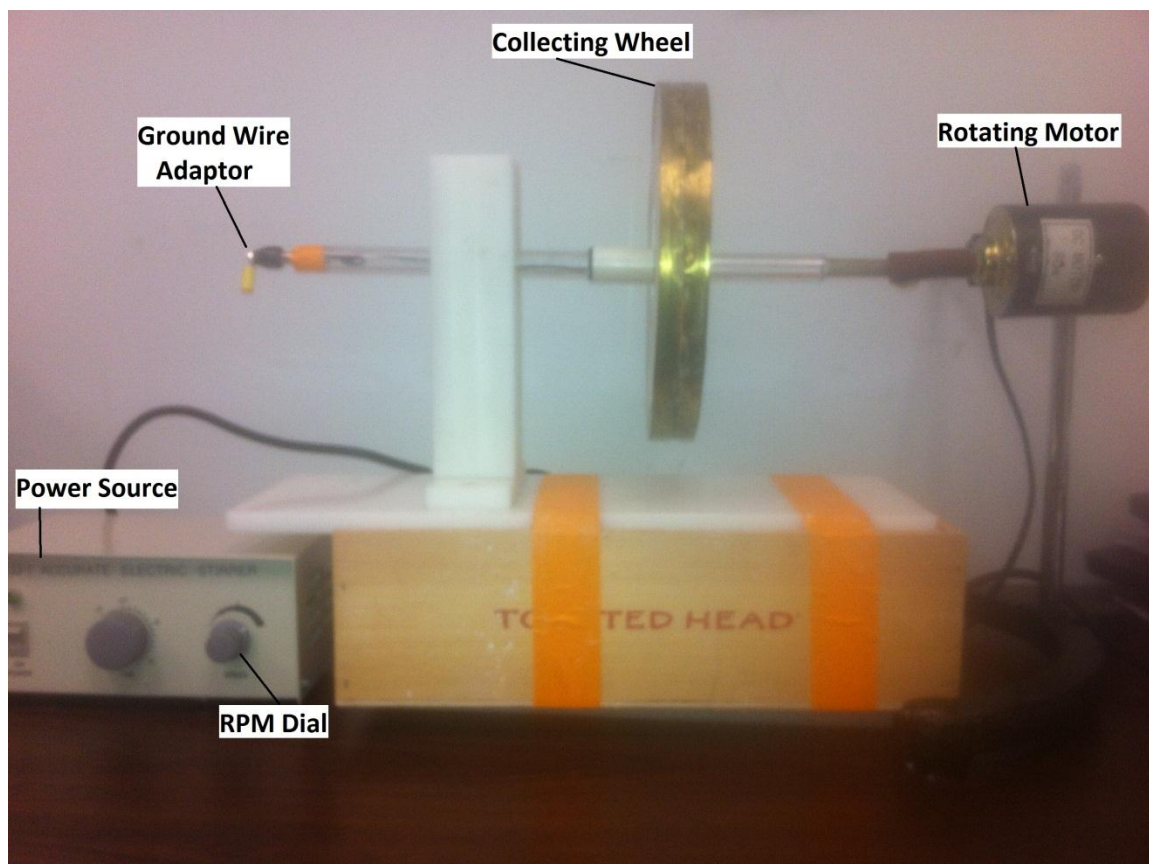
Figure 4.3 Diagram of rotating drum used for aligned electrospinning.

4.2.2 Scaffold Characterization

4.2.2.1 Visualizing Surface Morphology via SEM. In order to ensure each scaffold was created to the desired specifications, scanning electron microscopy (SEM) (LEO 1530 Gemini) was performed to test for the materials' fiber distribution, fiber diameter, and the degree of alignment. SEM served as the ideal tool due to its innate ability to generate high magnification 3-dimensional images with a superior resolution in comparison to a conventional microscope. Four samples were taken per scaffold for testing using biopsy punches (Miltex) to create disks measuring 6mm in diameter. They were then attached to aluminum mounts (Electron Microscopy Sciences) using double-sided carbon tape. To make the mounted samples conductive for SEM, they underwent a

gold-palladium coated sputtering process at 40mA for 15 seconds. The coated mounts were placed in the vacuum-sealed SEM chamber, with an accelerating voltage (electron high tension or EHT) of 3kV and a working distance (sample surface to lens) of 7-8mm. Four SEM images were each taken at 500X, 1KX, and 2.5KX, and then were analyzed using ImageJ software (National Institutes of Health).

4.2.2.2 Calculating Degree of Fiber Alignment.   Fiber alignment was determined by forming a line perpendicular to a fiber in each 1KX image (ImageJ). Five angle measurements were then taken at random between the drawn line and fiber, and their absolute deviation values were recorded (ADV). The following equation illustrates the needed   calculations   using   the   ADV   for   each   of   the   16   images:

$$\% \text{ Alignment} = (90° − ADV) / 90° * 100\% \tag{4.1}$$

4.2.2.3 Analyzing Fiber Thickness. In order to determine the fiber diameter for each scaffold, 1KX images were examined using ImageJ software. After globally standardizing the images using the scale bar, measurements were taken for five arbitrarily chosen fibers. These measurements were averaged for each image, then again for each scaffold type (20 images/per type) in order to determine the average fiber diameter.

4.2.3 OCT4-GFP BCCs

BCCs, transfected to express the OCT4 green fluorescent protein (OCT4-GFP), were supplied from several breast cancer patient donors at the University of Medicine and Dentistry of New Jersey (UMDNJ). Cell sorting yielded two breast cancer cell lines − those with high and low OCT4 expression levels − which were representative of

quiescent and active BCCs respectively. This transgene expression allowed for a straightforward and clear-cut view of the cells when viewed using confocal microscopy.

4.2.4 PicoGreen Cell Proliferation Assay

PicoGreen proliferation assays rely on comparing the absorbance levels of stained samples to that of known cell populations (standards). Standards were prepared by first suspending a thawed cryovial containing MSCs into a suspension of ~9mL general media/10^6 cells in a sterile environment. Next, the cells were centrifuged for six minutes at 1,300 rpm, the supernatant was removed, and the pellet was suspended in 1mL deionized H_2O (diH_2O). After determining the cell population using a hemacytometer (see section 4.2.4), the appropriate aliquots of cell suspension and diH_2O were transferred (see equation 4.2) into two sets of microcentrifuge tubes containing 0, 500, 1000, 2500, 5000, and 10000 cells respectively (total volume = 500μL). The ten standards were then transported – along with the study samples designated for analysis – to the assay room.

All standards were centrifuged in the Eppendorf miniSpin (2000rpm for 6min), rinsed in 500μL diH_2O, and centrifuged again, while designated samples were rinsed three times in 100μL diH_2O. After the rinsing stages, standards and samples were soaked in 100μL of 0.1% Triton X-100 in diH_2O for one hour at RT. Next, each sample was scraped for one minute using a pipette tip to dislodge any cells still attached to the scaffold/plate and then transferred (100μL) to a 96-well black fluorescent plate. The standards were pipetted thoroughly prior to transferring the 100μL suspensions. Lastly, 100μL of 1:200 PicoGreen Reagent in (1X TE Buffer) was added to each sample and standard and allowed to incubate in darkness for at least three minutes. Absorbance levels

were read using a FLx800 microplate fluorescence reader and KCjunior software (Bio-Tck Instruments) (excitation=480nm, emission=520nm, sensitivity=50).

4.2.5 Cell Fixation via Paraformaldehyde

Each sample underwent a cell fixing procedure in order to "freeze" the cells at their designated observation time point. Each sample was removed from the incubator, rinsed twice in PBS in sterile conditions, and transferred to the cell assay station. Afterwards, 100µL of 4% paraformaldehyde (Sigma-Alderich) diluted in PBS (pH=7.4) was then added and allowed to incubate at RT for twenty minutes. The samples were then rinsed twice in PBS, and soaked in 100µL of 0.1% Triton X in PBS for five minutes in order to permeablize the membrane for immunoassays. Finally, the samples were rinsed in PBS and were either wrapped in Parafilm® to be stored at 4°C, or set aside for cell stainings.

4.2.6 Cell Staining for Actin Filaments

This cytoskeletal staining was performed on samples containing either BCC or MSC cell types. Fixed, permeablized samples (Section 4.2.5) were soaked in 100µL of 1:100 rhodamine phalloidin (Invitrogen) in PBS for one hour at RT in darkness. They were then rinsed in PBS, wrapped in Parafilm®, and stored at 4°C to wait for analysis.

4.2.7 DAPI Nuclear Stain

The DAPI protocol for this study followed a near-identical procedure used in the *in vivo* bone regenerative analysis (Sub-subsection 3.2.1.3).

4.2.8 Confocal Microscopy

Stained samples were illuminated using three diode lasers with excitation values of 405 (blue), 488 (green), and 561 (red) nanometers. Images were recorded at either 20x or 40x magnification using NIS-Elements AR 3.2 software (Nikon). Each recorded image represents a compilation of confocal images of planes taken at various depths in the sample (z-stack) in order to render a clearer unobstructed view of a three-dimensional structure.

4.2.9 Statistical Analysis

All quantitative data underwent statistical processing identical to the methods discussed in the previous chapter/study (Section 3.2.3).

4.3   Results and Discussion

This section details the results for all experiments performed with the *in vitro* study. Discussed are the results for scaffold fabrication via electrospinning, both the BCC and MSC attachment to scaffold, cellular morphologies, and the cell viability of MSC-seeded scaffolds.

4.3.1 Scaffold Characterization

Eight different scaffolds were constructed for these series of experiments, varying in fiber orientation as well as composition. A 15%wt PCL in MC solution yielded two scaffold types – random and aligned fibrous mats. Random and aligned fiber scaffolds were also constructed from three composite materials obtained from solutions of 10%wt polymer PCL in MC combined with 30%wt ceramics of HA, β-TCP, and 20/80 ratio HA/β-TCP,

respectively. SEM imaging at 500X, 1000X, and 2500X revealed the fibrous micro and

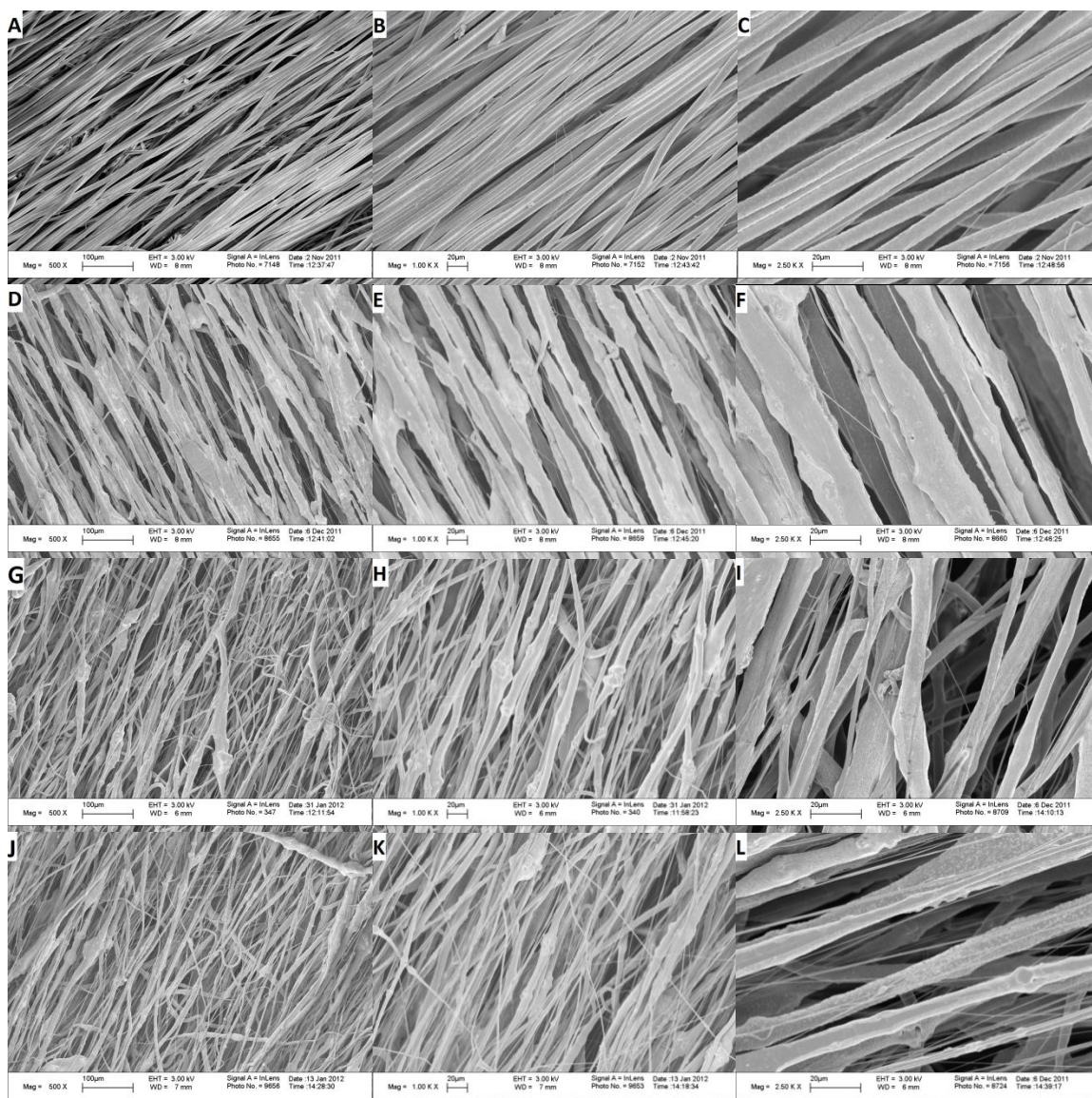nanostructures for each scaffold configuration and type (Figure 4.4-5).

Figure 4.4 SEM images taken at 500X, 1000X, and 2500X, respectively for PCL (A-C), PCL+HA (D-F), PCL+β-TCP (G-I), and PCL+β-TCP/HA (J-L) aligned fiber mats.
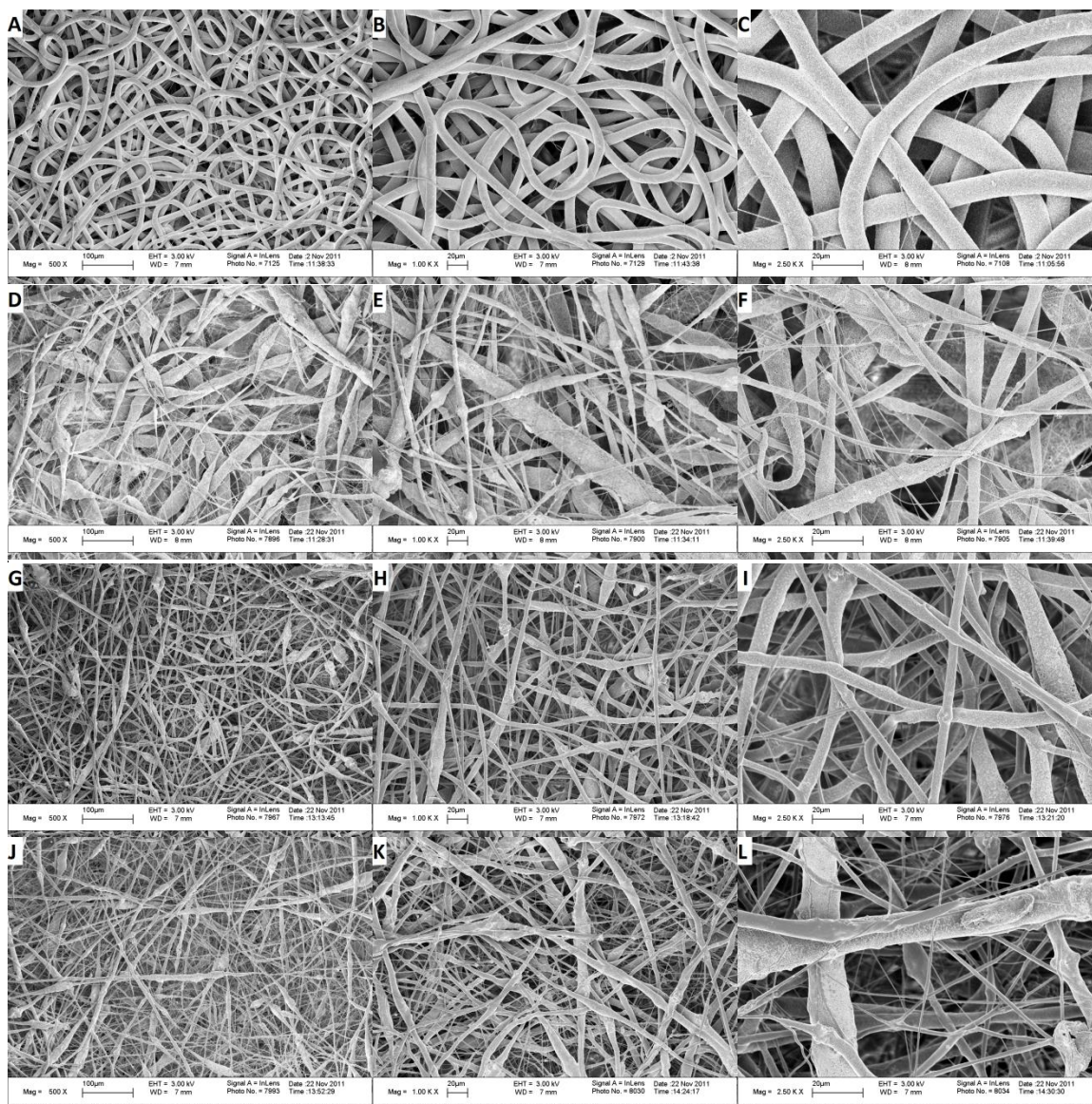
Figure 4.5 SEM images taken at 500X, 1000X, and 2500X, respectively for PCL (A-C), PCL+HA (D-F), PCL+β-TCP (G-I), and PCL+β-TCP/HA (J-L) random fiber mats.

Overall, the fibers for PCL random and aligned oriented mats are remarkably smoother in surface contours compared the composite scaffolds, where large ceramic granules are observed along the individual strands. These results are to be expected, as the ceramic nanoparticles tend to clump together when in solution despite the sonification process prior to spinning. This clumping in the composite mats also resulted in more variability in determining the fiber diameter. In Addition, for aligned fiber mats

containing β-TCP, there was an observable difference in the alignment compared to other aligned mat types. According to previous research, this could be attributed to residual charges left within the spun fibers on the collecting wheel [61, 62]. These charges, in turn, polarize the entire scaffold and deflect the ideal fiber alignment during the collection process. A visual observation during the electrospinning procedure noted the repellence of the electrospun fibers attempting to collect onto the grounded wheel, and instead deflecting back towards the syringe. This phenomenon appeared to be more typical as time went on and as the fibers continued to accumulate.

The average fiber diameters for each scaffold were calculated using the 1000X images (n=80) (Table 4.3). These measurements suggest with a 95% level of confidence that the true mean D_f of the scaffolds used in the series of experiments falls within these margins; however, the results are based upon the fabrication of only four scaffolds. The claim can be made that based upon sample size (n=4) the fiber diameters and alignments for all scaffold types are statistically similar.

Table 4.3 Fiber Diameters (Df) and Degree of Alignment for Electrospun Scaffolds

Fiber Type	Components	D_f (μm)	Alignment (%)
Random	PCL	9.54±2.23	
	PCL + HA	9.10±3.21	
	PCL + β-TCP	7.39±2.37	
	PCL + HA/β-TCP	7.99±3.23	
Aligned	PCL	8.86±2.13	95.41±4.78
	PCL + HA	9.92±2.93	95.90±3.27
	PCL + β-TCP	6.92±2.33	91.04±8.76
	PCL + HA/β-TCP	9.06±2.92	94.86±4.70

D_f = average ± standard deviation; fiber alignment calculated for aligned mats only; *PCL+β-TCP aligned electrospun mats had slightly smaller D_f compared to other aligned mats, but none of statistical significance (p<0.05).

The fiber diameters are influenced by a variety of factors such as viscosity, the voltage (V), flow rate (Q), and needle size [63]. For the case of PCL+β-TCP aligned fiber

scaffolds, a slight differences in D_f were noticed compared to other aligned mats, but not enough for any statistical significance (p<0.05). Slight differences would not be unexpected since although since β-TCP is less soluble compare to HA, which would result in a less uniform solution and create variability within the fiber strands. This non-uniformity could also affect the alignment of fibers. As discussed above, the resulting residual charge created by the electrospinning process could also lead to bends and loops within the fibrous scaffold. More exhaustive testing would need to be performed in order to increase the sample size and lower the variability in the standard deviations, creating a more reliable test statistic. In addition, methods of solution preparation need to be more effective towards creating a homogenous solution with minimal ceramic aggregates.

4.3.2 BCC Attachment and Morphology

Both BCC-lines were both exposed to the nuclear DAPI stain, and phalloidin was applied to highlight the cell morphology using actin filaments. Confocal images were then taken at 40x magnification of each cell type on every scaffold, for all time points (Figures 4.6-4.7). For composite scaffolds (Figures 4.6-7:B,C,F,G), ceramic debris can be seen, appearing as reddish blobs that indicate aggregates within the fibers. This is to be expected, as SEM imaging also confirms the non-uniformity when using ceramic components. Also as expected, scaffolds comprised of β-TCP portray more aggregates than composites containing only HA (Figure 4.7C,G) since β-TCP is known to be less soluble.
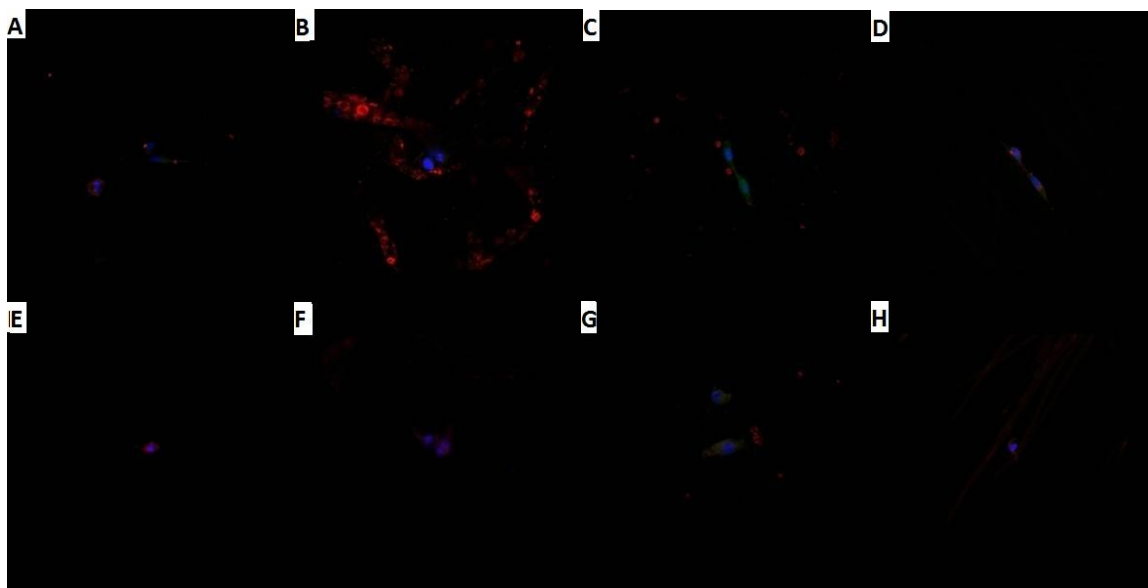
Figure 4.6 Confocal images taken at 40x magnification on day 1 (A-D) and 4 (E-H) of MD cells with Oct4-Hi expression seeded on PCL, PCL+HA, PCL+β-TCP, and aligned PCL scaffolds respectively. Nuclear-stain DAPI (blue) is surrounded by the cell's actin filaments (red) and GFP-Oct4 (green); scaffold debris is also seen (red).

Figure 4.7 Confocal images taken at 40x magnification on day 1 (A-D) and 4 (E-H) of MD cells with Oct4-Lo expression seeded on PCL, PCL+HA, PCL+β-TCP, and aligned PCL scaffolds respectively. Nuclear-stain DAPI (blue) is surrounded by the cell's actin filaments (red) and GFP-Oct4 (green); scaffold debris is also seen (red).
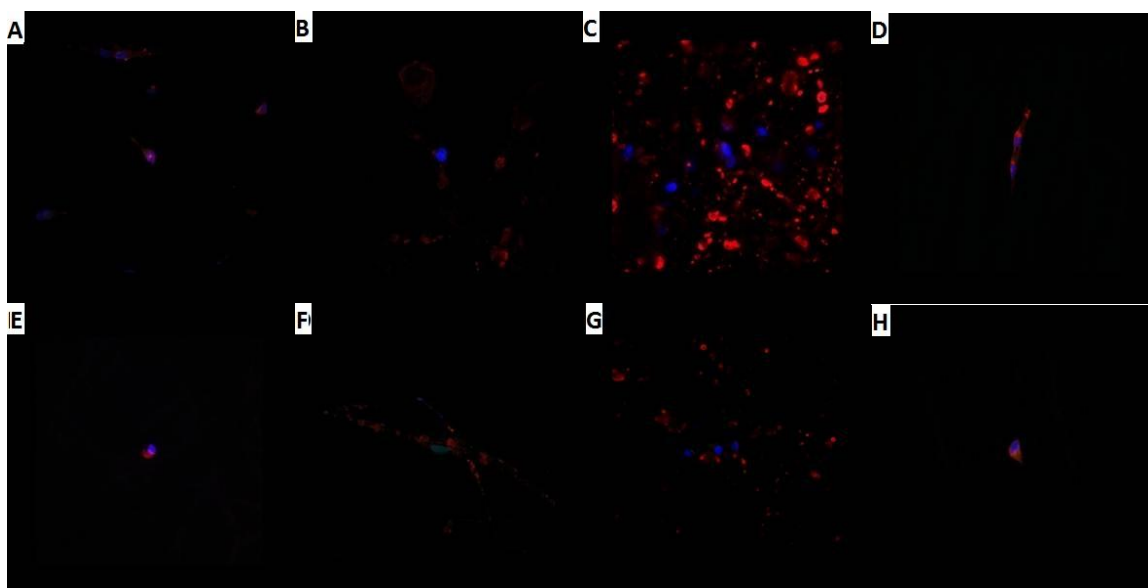
Perhaps the most interesting observation within the BCC images is the expression of the OCT4-GFP. In samples containing Oct4-Hi BCCs (Figure 4.6), traces of OCT-4

can be seen at day 1; however, by day 4 the samples containing PCL only (images E and H) showed no OCT-4 expression, suggesting that the BCCs were becoming more aggressive. The same scenario holds true even for Oct4-Lo BCCs (Figure 4.8), where day 4 confocal images show OCT4-GFP for ceramic composite scaffolds, but not for PCL alone. This observation is highly important for Oct4-Lo cells since the emergence of OCT-4 signifies BCCs entering a state of dormancy. Therefore, it can be suggested that composite scaffolds containing polymer and ceramic components support the less aggressive Oct4-Hi BCCs, which is necessary in studying breast cancer dormancy.

4.3.3 MSC Attachment and Morphology

Two confocal images were captured for each sample at every time point, which highlights the cell nuclei (blue), actin filaments (red), and scaffold fibers that are picked up in the background noise. The 488nm (green) laser was not necessary for this study, as no antibodies fluoresced at that wavelength. The following compilation of images (Figures 4.8-12) provides only an examination of the seeded cells, and they are not an accurate example of the scaffold as a whole. This could be attributed to specific methods described within the cell seeding protocol in which the cell suspension was pipetted onto a localized area of the scaffold sitting in general media, which was not mixed uniformly afterwards. Therefore, in day 1 samples, MSCs appeared numerous in selective locations while being absent entirely from others on a given scaffold.

In Figures 4.8-4.11, drastic differences in actin filaments were observed between random (A-D) and the aligned (E-H) fiber mats. In confocal images of randomly oriented scaffolds, actin filaments were not as pronounced, particularly at day 1. At days 7 and 14, MSCs were given more time to form attachments and elongate on the scaffolds. As a

result, the actin began to branch out into box-like structures that filled the inter-fiber spacings, and formed attachments to adjacent fibers.

In the images containing aligned fiber scaffolds (Figures 4.8-11:E-H), the actin appeared to take on a more unified role. As early as day 1, actin filaments began to stretch, indicating cell elongation along the fibers. Previous literature suggests a connection between observed cell elongation and cell migration [13, 14]. This process ultimately would prove useful in the guidance of bone formation as well as the formation of aligned mineralized collagen fibrils, which make up the majority of bone. For images containing ceramic components (Figures 4.9-4.11), HA and β-TCP particles were picked up by the red confocal laser, which add to the background noise. They are typically seen as globular masses which follow the same patterning trend as the electrospun fibers. Lastly, the tissue-plated samples that act as the controls for the experiments (Figure 4.12) quickly formed a confluent monolayer by day 7, forming laterally-wide flattened actin filaments clinging to the surface of the culture-treated well. This result was expected since the cells could only attach in one dimension as opposed to the porous architecture created by the fibers. On day 4 of the control (Figure 4.12D) the actin self-oriented into an aligned pattern.
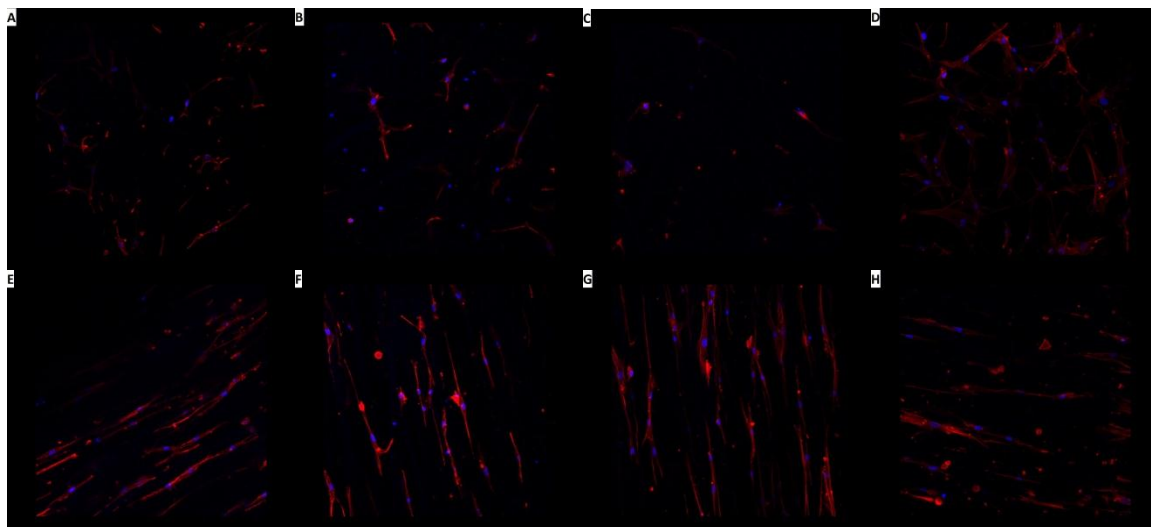
Figure 4.8 Confocal images taken at 20x of MSCs seeded on random PCL (A-D) and aligned PCL (E-H) scaffolds at days 1, 4, 7, and 14, respectively.
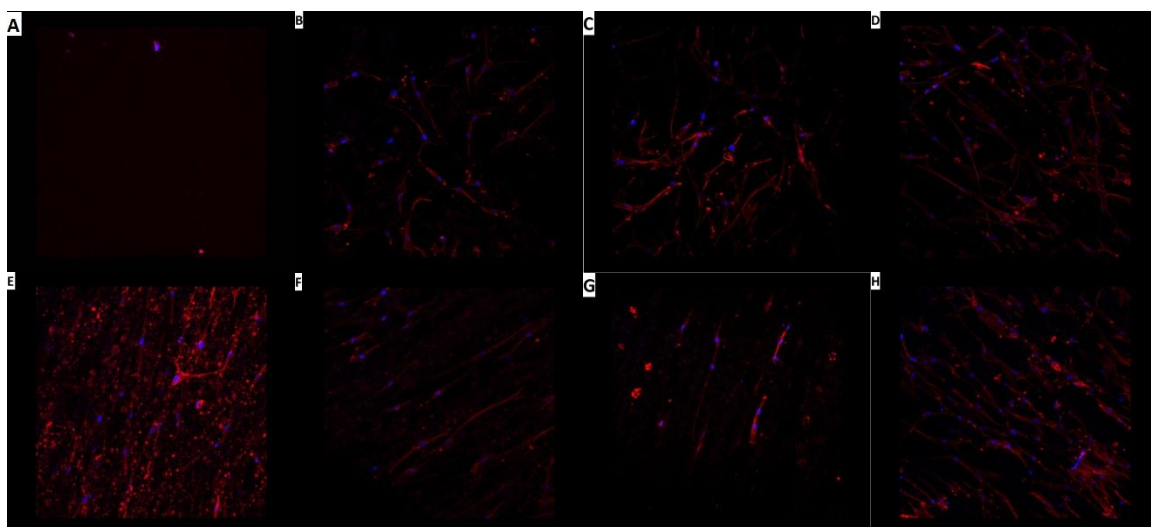

Figure 4.9 Confocal images taken at 20x of MSCs seeded on random PCL+HA (A-D) and aligned PCL+HA (E-H) scaffolds at days 1, 4, 7, and 14, respectively.
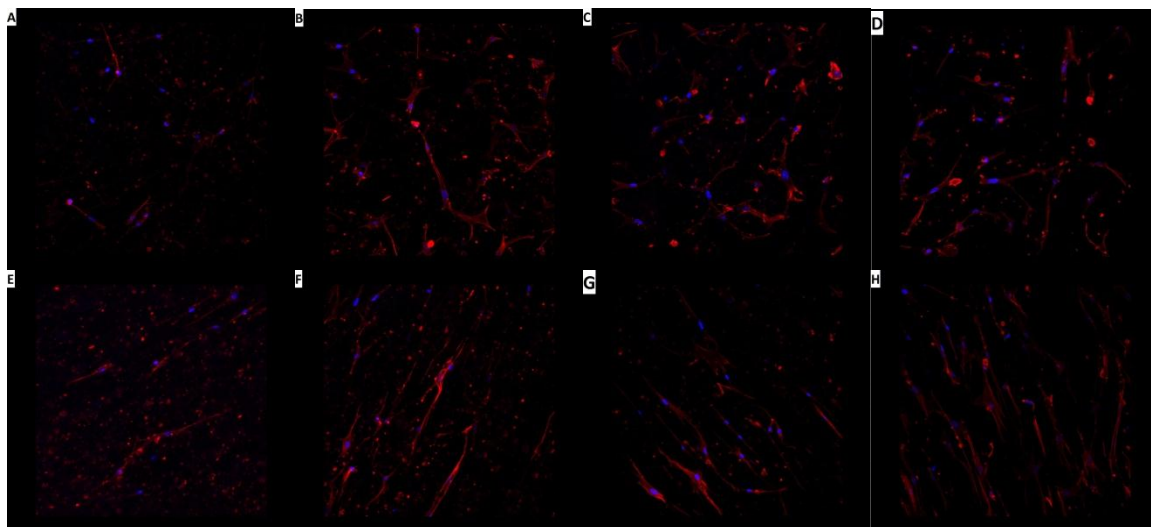
Figure 4.10 Confocal images taken at 20x of MSCs seeded on random PCL+β-TCP (A-D) and aligned PCL+β-TCP (E-H) scaffolds at days 1, 4, 7, and 14, respectively.
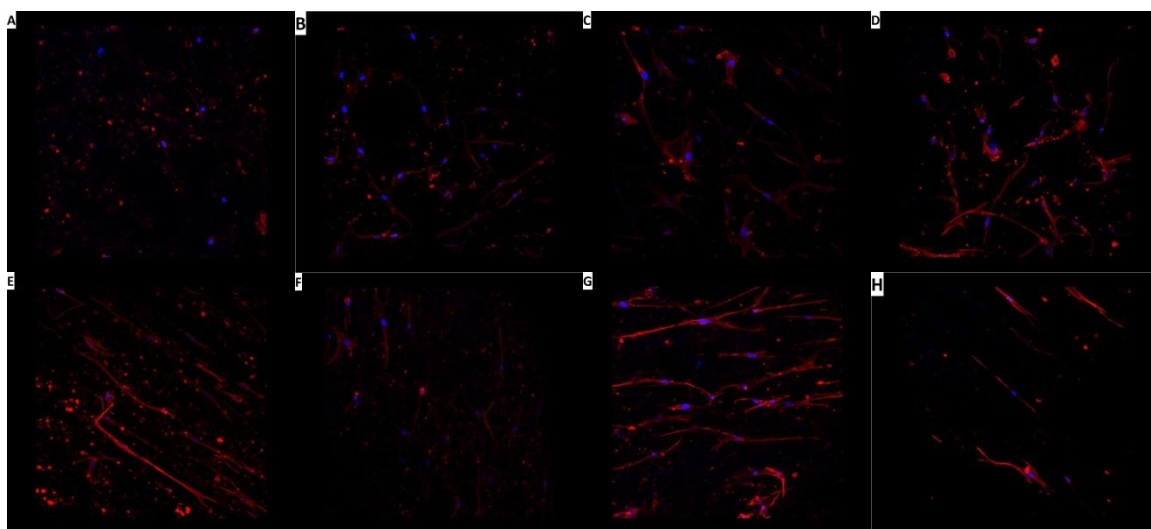

Figure 4.11 Confocal images taken at 20x of MSCs seeded on random PCL+β-TCP/HA (A-D) and aligned PCL+β-TCP/HA (E-H) scaffolds at days 1, 4, 7, and 14, respectively.
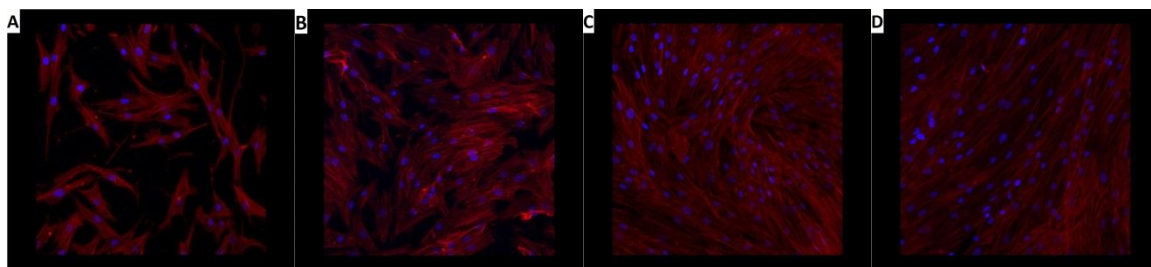

Figure 4.12 Confocal images taken at 20x of MSCs seeded on tissue culture plates (control) at days 1, 4, 7, and 14, respectively.

4.3.4 MSC Proliferation Assay

At times points day 1, 4, 7, and 14, MSCs seeded at 1000cells/sample onto each scaffold (n=4) were analyzed to determine the population count by following the PicoGreen Assay protocol (Section 4.2.4). The results were then calculated based upon the plate readouts and generated standard curves, and the values were graphed depicting the rate of growth for each scaffold over a two week period. Figures 4.13-4.16 show an overlaid comparison between aligned and random fiber oriented scaffolds for each composition; the computed standard deviations were included as error bars to demonstrate the variability of each value. Statistical analysis revealed significantly higher cell counts for random fiber mats compared to aligned fiber mats at days 1 and 4 for all compositions. This difference, primarily at day 1, suggests that initial cell attachment is favorable for random fiber mats. This result could be based upon several factors such as interfiber spacing, cell seeding errors, and the ability for cells to penetrate the scaffolds. If fiber spacing is too small, then cells may not have enough surface area to attach or penetrate the scaffold surface.

The control is shown, both on its own (Figure 4.17) and overlaid with the PicoGreen data for all scaffold compositions and types (Figure 4.18). Figure 4.19 provides a closer comparison of MSCs seeded on all scaffolds by removing the control data. At days 1, 4, and 7, all random fiber scaffolds recorded high cell populations in comparison to aligned fiber-oriented scaffolds of the same material composition. This difference appears most prominent at day 1, indicating differences in initial cell attachment to the scaffold. At day 14 (week 2), aligned fiber scaffolds containing β-TCP were noted as having high cell numbers than their aligned counterparts, however, the

overlapping within the standard deviations prevents any significant conclusions from being drawn. Control MSCs grown on treated tissue culture plates experienced a sharp incline between day 7 and 14 with minimal deviation according to the charted data. At this point, it is important to note that time-points on the horizontal x-axis are not proportionately distributed; therefore, the visual representation of the line graph between day 7 and 14 is intrinsically slightly distorted.

Several data points in the results did not fit the expected trends for the experiment. For example, in day 14 of the random scaffolds containing β-TCP, and particularly the aligned PCL scaffold, there was a decrease observed in the cell population count. In addition, as previously mentioned (Section 4.3.3) the cells were not seeded uniformly onto the scaffolds, but rather were transferred from a condensed suspension onto a localized area of the scaffold. This could potentially have created experimental errors in the cell attachments and lead to larger variances within the data.

Overall, repeated testing is needed in order to confirm the validity of these results. Furthermore, sequential research would investigate behaviors such as MSC osteogenic behavior using well-known protein markers such as alkaline phosphatase and calcium. If certain scaffolds were found to induce osteogenesis in MSCs at an earlier stage, then the proliferation assays could be affected, since cell growth ceases at the point of differentiation.
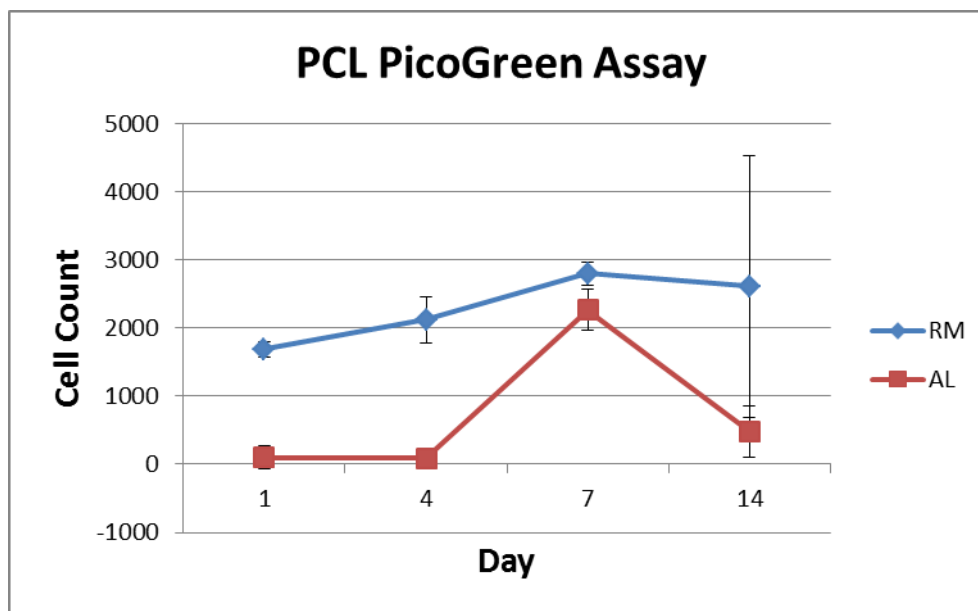
Figure 4.13 Graph comparing MSC cell counts for aligned (red) versus random (blue) fiber PCL scaffolds.
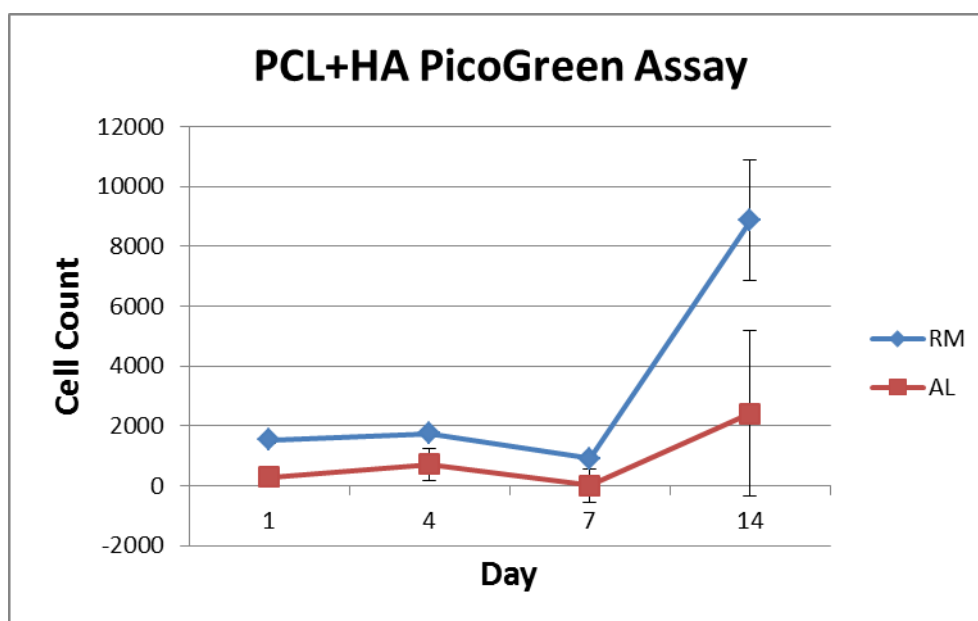

Figure 4.14 Graph comparing MSC cell counts for aligned (red) versus random (blue) fiber PCL+HA scaffolds.

Figure 4.15 Graph comparing MSC cell counts for aligned (red) versus random (blue) fiber PCL+β-TCP scaffolds.
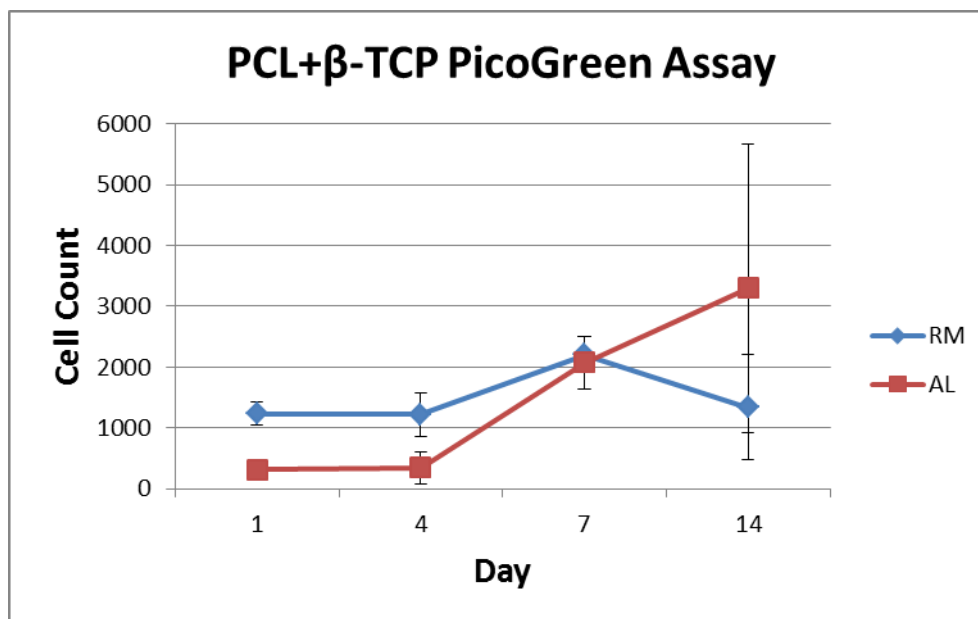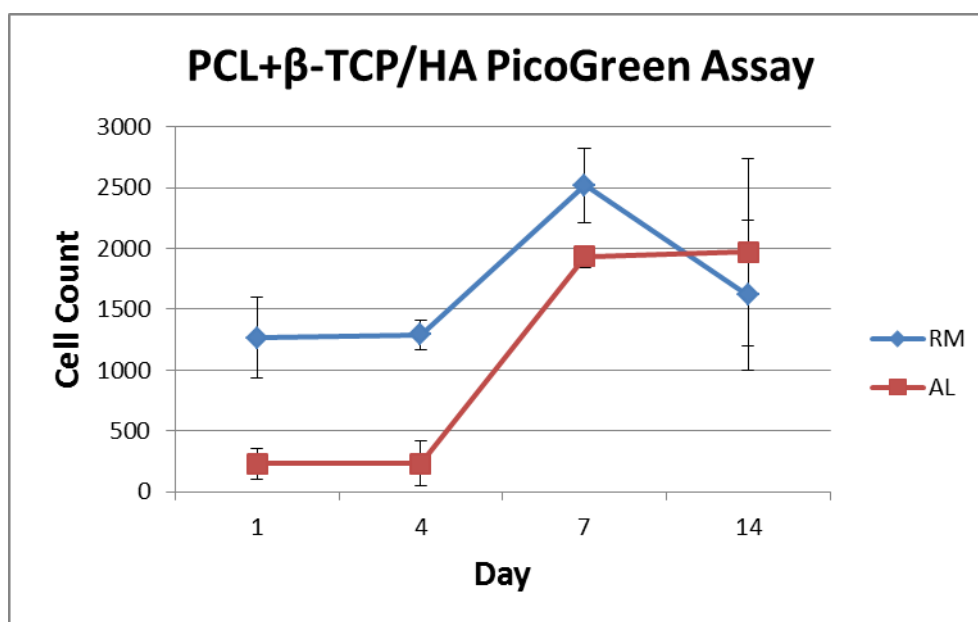

Figure 4.16 Graph comparing MSC cell counts for aligned (red) versus random (blue) fiber PCL+β-TCP/HA scaffolds.
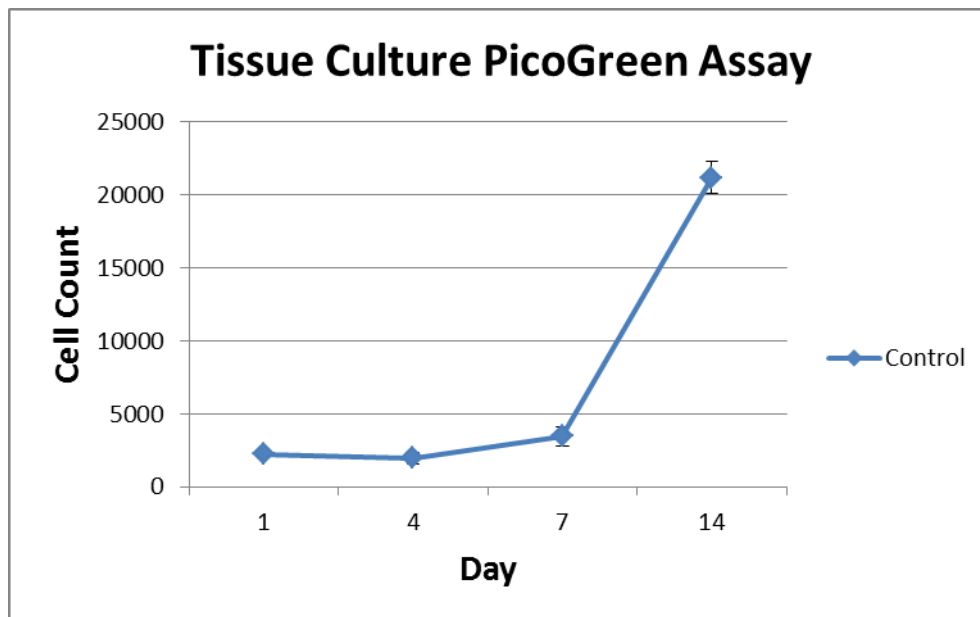
Figure 4.17 Graph displaying MSC cell counts for control group seeded on a culture-treated plate.
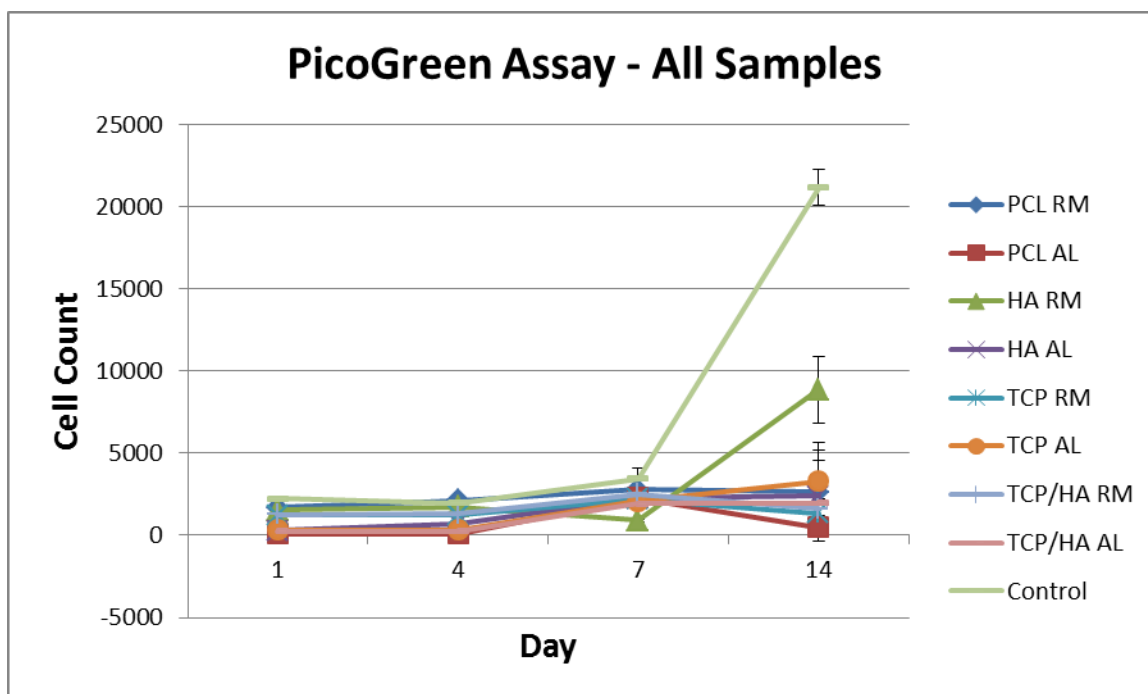

Figure 4.18 Graph displaying MSC cell population counts for all seeded samples.
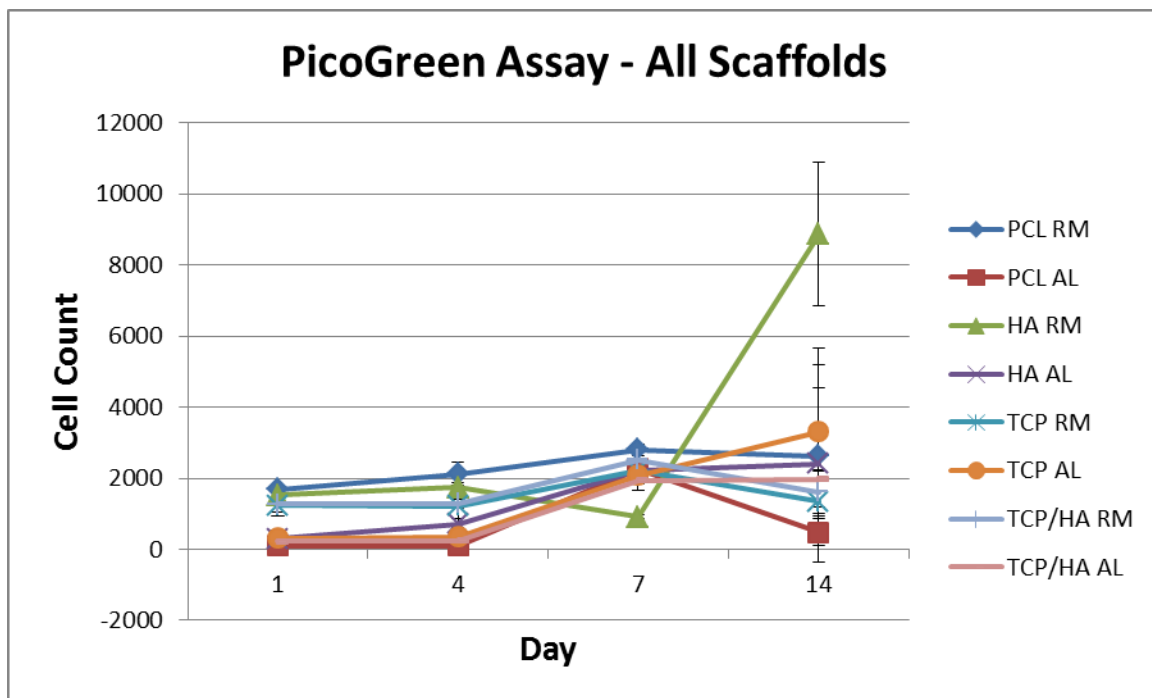
Figure 4.19 Graph of MSC cell population counts for scaffolds only (no control).

CHAPTER 5

CONCLUSION

The two main experiments, although different in their designed purpose, both demonstrate practical applications for bone tissue engineering techniques. Whether the intended goal is to advance tissue regeneration in orthopaedic surgeries, or to design a construct capable of examining cellular interactions, tissue engineering strategies can be developed in order to meet the needs and specifications.

Extensive immunohistochemical analysis revealed intriguing results for the *in vivo* VAC therapy study on the New Zealand rabbit subjects. Semi-quantitative results indicated significantly improved rates of tissue regrowth (via BrdU expression) in week 1 subjects who received the experimental VAC treatment. Furthermore, ALP analysis suggests superior osteoconductive behavior compared to rabbits who did not receive the treatment. Therefore, vacuum-assisted wound closure could hold promise in orthopaedic surgical procedures as a method to promote tissue and bone regrowth. Further preclinical trials would need to be conducted in order to more definitively validate these findings before moving forward to clinical experiments in human patients. Furthermore, since the particular secondary treatment involving the porous ceramic scaffold was not favorable with VAC therapy, other orthopedic treatments could be tested for use in combination for surgeries.

Significant progress was also made in creating a viable tissue-engineered biomimetic bone scaffold for both MSCs and BCCs; however, more groundwork still needs to be laid concerning cell viability. Results did indicate favorability for Oct4-Hi BCCs towards composite scaffolds, which is preferable for studying BCC dormancy.

Further research would test the biocompatibility of BCCs all aligned composite scaffold compositions prior to a main investigative study examining the intracellular mechanisms between the two cell lines. In addition, the intrinsic osteogenic properties of the scaffolds needs to be tested utilizing an osteoinductive media in order to better initiate the differentiation process that would naturally occur within the body. Methods also need to be developed in which to simultaneously visualize markers for both cell types, their structures, and other potential protein markers. Lastly, fabrication methods need to be refined in order to create scaffolds with better alignment (particularly for ceramic scaffolds) and with high levels of fiber uniformity.

REFERENCES

1. Langer, R. and J.P. Vacanti, *Tissue engineering.* Science, 1993. **260**(5110): p. 920-6.

2. MacArthur, B.D. and R.O. Oreffo, *Bridging the gap.* Nature, 2005. **433**(7021): p. 19.

3. Hing, K.A., *Bone repair in the twenty-first century: biology, chemistry or engineering?* Philos Transact A Math Phys Eng Sci, 2004. **362**(1825): p. 2821-50.

4. *Bone Basics: Fast Facts*. 2011, International Osteoporosis Foundation.

5. *Orthopedics: Fractures*. Hospital-Services 2012; Available from: http://www.centennialhillshospital.com/Hospital-Services/Orthopedics.

6. Laurencin CT, K.Y., *Bone Graft Substitute Materials*, in *eMedicine.com Inc*. 2006.

7. Cooley, J., *Apparatus for electrically dispersing fluids*, U.S.P. Office, Editor. 1902.

8. Jang, J.-H., O. Castano, and H.-W. Kim, *Electrospun materials as potential platforms for bone tissue engineering.* Advanced Drug Delivery Reviews, 2009. **61**(12): p. 1065-1083.

9. Woo, K.M., et al., *Nano-fibrous scaffolding promotes osteoblast differentiation and biomineralization.* Biomaterials, 2007. **28**(2): p. 335-43.

10. Chew, S.Y., et al., *Aligned Protein-Polymer Composite Fibers Enhance Nerve Regeneration: A Potential Tissue-Engineering Platform.* Adv Funct Mater, 2007. **17**(8): p. 1288-1296.

11. Peng, F., X. Yu, and M. Wei, *In vitro cell performance on hydroxyapatite particles/poly(L-lactic acid) nanofibrous scaffolds with an excellent particle along nanofiber orientation.* Acta Biomater, 2011. **7**(6): p. 2585-92.

12. Lu, L.X., et al., *The effects of PHBV electrospun fibers with different diameters and orientations on growth behavior of bone-marrow-derived mesenchymal stem cells.* Biomed Mater, 2012. **7**(1): p. 015002.

13. Agudelo-Garcia, P.A., et al., *Glioma cell migration on three-dimensional nanofiber scaffolds is regulated by substrate topography and abolished by inhibition of STAT3 signaling.* Neoplasia, 2011. **13**(9): p. 831-40.

14. Wang, Y., et al., *Biocompatibility evaluation of electrospun aligned poly (propylene carbonate) nanofibrous scaffolds with peripheral nerve tissues and cells in vitro.* Chin Med J (Engl), 2011. **124**(15): p. 2361-6.

15. Valarmathi, M.T., et al., *A three-dimensional tubular scaffold that modulates the osteogenic and vasculogenic differentiation of rat bone marrow stromal cells.* Tissue Eng Part A, 2008. **14**(4): p. 491-504.

16. Cai, Y.Z., et al., *Novel biodegradable three-dimensional macroporous scaffold using aligned electrospun nanofibrous yarns for bone tissue engineering.* J Biomed Mater Res A, 2012. **100**(5): p. 1187-94.

17. Wang, Y., et al., *The differential effects of aligned electrospun PHBHHx fibers on adipogenic and osteogenic potential of MSCs through the regulation of PPARgamma signaling.* Biomaterials, 2012. **33**(2): p. 485-93.

18. Cao, H., T. Liu, and S.Y. Chew, *The application of nanofibrous scaffolds in neural tissue engineering.* Advanced Drug Delivery Reviews, 2009. **61**(12): p. 1055-1064.

19. Moore, M.J., et al., *Multiple-channel scaffolds to promote spinal cord axon regeneration.* Biomaterials, 2006. **27**(3): p. 419-429.

20. Tabesh, H., et al., *The role of biodegradable engineered scaffolds seeded with Schwann cells for spinal cord regeneration.* Neurochemistry International, 2009. **54**(2): p. 73-83.

21. Willerth, S.M. and S.E. Sakiyama-Elbert, *Approaches to neural tissue engineering using scaffolds for drug delivery.* Advanced Drug Delivery Reviews, 2007. **59**(4-5): p. 325-338.

22. Fong, P., et al., *The use of polymer based scaffolds in tissue-engineered heart valves.* Progress in Pediatric Cardiology, 2006. **21**(2): p. 193-199.

23. Hidalgo-Bastida, L.A., et al., *Cell adhesion and mechanical properties of a flexible scaffold for cardiac tissue engineering.* Acta Biomaterialia, 2007. **3**(4): p. 457-462.

24. Yeong, W.Y., et al., *Porous polycaprolactone scaffold for cardiac tissue engineering fabricated by selective laser sintering.* Acta Biomaterialia, 2010. **6**(6): p. 2028-2034.

25. Hammond, J.S., et al., *Optimisation of a polymer scaffold for liver tissue engineering.* Journal of Surgical Research, 2006. **130**(2): p. 300.

26. Jiang, J., et al., *Cultivation and induction of fetal liver cells in poly-l-lactic acid scaffold.* Materials Science and Engineering: C, 2004. **24**(3): p. 361-363.

27. Drosse, I., et al., *Tissue engineering for bone defect healing: An update on a multi-component approach.* Injury, 2008. **39, Supplement 2**(0): p. S9-S20.

28. Livingston, T., P. Ducheyne, and J. Garino, *In vivo evaluation of a bioactive scaffold for bone tissue engineering.* J Biomed Mater Res, 2002. **62**(1): p. 1-13.

29. Bucholz, R.W., *Nonallograft osteoconductive bone graft substitutes.* Clin Orthop Relat Res, 2002(395): p. 44-52.

30. Gleeson, J.P., N.A. Plunkett, and F.J. O'Brien, *Addition of hydroxyapatite improves stiffness, interconnectivity and osteogenic potential of a highly porous collagen-based scaffold for bone tissue regeneration.* Eur Cell Mater, 2010. **20**: p. 218-30.

31. Venkatesan, J. and S.K. Kim, *Chitosan composites for bone tissue engineering--an overview.* Mar Drugs, 2010. **8**(8): p. 2252-66.

32. Ugo, R., *Osteoinduction in porous hydroxyapatite implanted in heterotopic sites of different animal models.* Biomaterials, 1996. **17**(1): p. 31-35.

33. Le Guehennec, L., P. Layrolle, and G. Daculsi, *A review of bioceramics and fibrin sealant.* Eur Cell Mater, 2004. **8**: p. 1-10; discussion 10-1.

34. (2008) *Bone Grafts and Bone Substitutes*. Orthopedic Network News **19**, 4.

35. Elliott, J., R. Wilson, and S. Dowker, *Structure and Chemistry of the Apatites and Other Calcium Orthophosphates.* Elsevier, 1994.

36. Habraken, W.J.E.M., J.G.C. Wolke, and J.A. Jansen, *Ceramic composites as matrices and scaffolds for drug delivery in tissue engineering.* Advanced Drug Delivery Reviews, 2007. **59**(4-5): p. 234-248.

37. Arinzeh, T.L., et al., *A comparative study of biphasic calcium phosphate ceramics for human mesenchymal stem-cell-induced bone formation.* Biomaterials, 2005. **26**(17): p. 3631-8.

38. Roohani-Esfahani, S.I., et al., *Effect of self-assembled nanofibrous silk/polycaprolactone layer on the osteoconductivity and mechanical properties of biphasic calcium phosphate scaffolds.* Acta Biomater, 2011.

39. Lu, H.H., et al., *Compositional effects on the formation of a calcium phosphate layer and the response of osteoblast-like cells on polymer-bioactive glass composites.* Biomaterials, 2005. **26**(32): p. 6323-34.

40. Liu, X. and P.X. Ma, *Polymeric scaffolds for bone tissue engineering.* Ann Biomed Eng, 2004. **32**(3): p. 477-86.

41. Lao, L., et al., *Poly(lactide-co-glycolide)/hydroxyapatite nanofibrous scaffolds fabricated by electrospinning for bone tissue engineering.* J Mater Sci Mater Med, 2011. **22**(8): p. 1873-84.

42. Francis, L., et al., *Simultaneous electrospin-electrosprayed biocomposite nanofibrous scaffolds for bone tissue regeneration.* Acta Biomater, 2010. **6**(10): p. 4100-9.

43. Patlolla, A., G. Collins, and T.L. Arinzeh, *Solvent-dependent properties of electrospun fibrous composites for bone tissue regeneration.* Acta Biomater, 2010. **6**(1): p. 90-101.

44. Zhang, Z., et al., *Osteoinduction with HA/TCP Ceramics of Different Composition and Porous Structure in Rabbits.* Oral Science International, 2005. **2**(2): p. 85-95.

45. Huang, Y., et al., *Effect of cyclic strain on cardiomyogenic differentiation of rat bone marrow derived mesenchymal stem cells.* PLoS One, 2012. **7**(4): p. e34960.

46. Birmingham, E., et al., *Osteogenic differentiation of mesenchymal stem cells is regulated by osteocyte and osteoblast cells in a simplified bone niche.* Eur Cell Mater, 2012. **23**: p. 13-27.

47. Ayatollahi, M., et al., *Hepatogenic differentiation of mesenchymal stem cells induced by insulin like growth factor-I.* World J Stem Cells, 2011. **3**(12): p. 113-21.

48. Hernandez-Benitez, R., G. Ramos-Mandujano, and H. Pasantes-Morales, *Taurine stimulates proliferation and promotes neurogenesis of mouse adult cultured neural stem/progenitor cells.* Stem Cell Res, 2012. **9**(1): p. 24-34.

49. Bordei, P., *Locally applied platelet-derived growth factor accelerates fracture healing.* J Bone Joint Surg Br, 2011. **93**(12): p. 1653-9.

50. Graham, A. and J. Rosner, *Complex monolithic optics enrich fluorescence imaging*. 2008, BioOptics World.

51. Ekstrom, P. *Facts about confocal laser microscopy*. Confocal Microscopy 2011; Available from: http://www.biologi.lu.se/services/confocal-microscopy/facts-about-confocal-microscopy.

52. Neves, N.M., et al., *Patterning of polymer nanofiber meshes by electrospinning for biomedical applications.* Int J Nanomedicine, 2007. **2**(3): p. 433-48.

53. Polini, A., et al., *Osteoinduction of Human Mesenchymal Stem Cells by Bioactive Composite Scaffolds without Supplemental Osteogenic Growth Factors.* PLoS One, 2011. **6**(10): p. e26211.

54. Jacobs, S., et al., *Efficacy and mechanisms of vacuum-assisted closure (VAC) therapy in promoting wound healing: a rodent model.* J Plast Reconstr Aesthet Surg, 2009. **62**(10): p. 1331-8.

55. Dedmond, B.T., et al., *The use of negative-pressure wound therapy (NPWT) in the temporary treatment of soft-tissue injuries associated with high-energy open tibial shaft fractures.* J Orthop Trauma, 2007. **21**(1): p. 11-7.

56. Patel, S.A., et al., *Breast cancer biology: the multifaceted roles of mesenchymal stem cells.* J Oncol, 2008. **2008**: p. 425895.

57. Lim, P.K., et al., *Gap junction-mediated import of microRNA from bone marrow stromal cells can elicit cell cycle quiescence in breast cancer cells.* Cancer Res, 2011. **71**(5): p. 1550-60.

58. Patel, S.A., et al., *Metastatic breast cancer cells in the bone marrow microenvironment: novel insights into oncoprotection.* Oncol Rev, 2011. **5**(2): p. 93-102.

59. Patel, S.A., et al., *Immunological properties of mesenchymal stem cells and clinical implications.* Arch Immunol Ther Exp (Warsz), 2008. **56**(1): p. 1-8.

60. Patel, S.A., et al., *Mesenchymal stem cells protect breast cancer cells through regulatory T cells: role of mesenchymal stem cell-derived TGF-beta.* J Immunol, 2010. **184**(10): p. 5885-94.

61. Catalani, L.H., G. Collins, and M. Jaffe, *Evidence for Molecular Orientation and Residual Charge in the Electrospinning of Poly(butylene terephthalate) Nanofibers.* Macromolecules, 2007(40): p. 1693-1697.

62. Collins, G., et al., *Charge generation, charge transport, and residual charge in the electrospinning of polymers: A review of issues and complications.* Journal of Applied Physics, 2012. **111**(4): p. 18.

63. Fridrikh, S.V., et al., *Controlling the fiber diameter during electrospinning.* Phys Rev Lett, 2003. **90**(14): p. 144502.